095028
(19)

JOURNAL OF GEOPHYSICAL RESEARCH, VOL. 111, B09201, doi:10.1029/2005JB003892, 2006

Click Here for Full Article

Correction published 9 November 2006

Diagenesis of deformation band faults: Record and mechanical consequences of vadose zone flow and transport in the Bandelier Tuff, Los Alamos, New Mexico

Jennifer E. Wilson,[1] Laurel B. Goodwin,[2] and Claudia Lewis[3]

DOE ... DATES
MAR 1 2 2007
By

Received 20 June 2005; revised 8 March 2006; accepted 19 May 2006; published 6 September 2006.

[1] Deformation band faults in nonwelded ignimbrites of the Bandelier Tuff record unsaturated fluid flow and transport. More than two thirds of the faults studied display diagenetic minerals virtually absent from adjacent protolith. Stable isotope analyses indicate that smectite enrichment and calcite cementation result from low-temperature meteoric fluid-fault interaction. Fault zone microstructures, rare earth element signatures, and mineralogy indicate that smectite was introduced to deformation band fault zones by a combination of translocation from the surface and in situ alteration of fault gouge. Rod-shaped calcite microcrystallites and the close association of calcite with plant roots suggest a combination of pedogenic, biologically mediated, and physicochemical precipitation. Enrichment in smectite and calcite modified major oxide and trace element contents of deformation bands with respect to protolith. Collectively, these observations indicate that these faults have served as, and may still be, zones of preferential vadose zone fluid flow and transport. These processes alter fault rock permeability; affect the transport of solutes via processes such as dissolution, precipitation, and adsorption, and they change the mechanical properties of the fault zone. Smectite and calcite enrichment results in localization of deformation, effectively halting the further development of deformation bands. Vadose zone alteration therefore is one way to produce a clay-rich fault core at early stages in a fault's history, resulting in fault zone weakening and localization of slip. Progressive burial of growth faults can subsequently bring fault cores into the seismogenic zone.

Citation: Wilson, J. E., L. B. Goodwin, and C. Lewis (2006), Diagenesis of deformation band faults: Record and mechanical consequences of vadose zone flow and transport in the Bandelier Tuff, Los Alamos, New Mexico, *J. Geophys. Res.*, *111*, B09201, doi:10.1029/2005JB003892.

1. Introduction

[2] The interaction between fluid flow and faulting is complex and involves an incompletely understood combination of processes. One approach to understanding these processes is to measure the hydrologic properties (e.g., porosity and permeability) of fault rock with respect to protolith [e.g., *Antonellini and Aydin*, 1994; *Sigda et al.*, 1999; *Rawling et al.*, 2001; *Dinwiddie et al.*, 2002; *Sigda and Wilson*, 2003]. This approach usually requires sophisticated equipment, large amounts of data, and time-consuming data reduction and correction algorithms [e.g., *Aronson*, 1999; *Tidwell and Wilson*, 2000]. Another useful way to evaluate the interaction between faulting and fluid flow is to integrate microstructural characterization with the diagenetic record of flow found in, versus adjacent to, fault rock [e.g., *Knipe*, 1993; *Evans and Chester*, 1995; *Mozley and Goodwin*, 1995]. In this approach, microstructural analysis of fault zone material characterizes the pores and pathways through which fluids move through fault rock. Geochemical analyses of variably altered fault material can help identify fault zones as conduits, barriers, or complex conduit-barrier systems [e.g., *Caine et al.*, 1996; *Tobin et al.*, 2001].

[3] Faults can be grouped into a variety of classes, including large- versus small-displacement faults and those that are dominated by fractures versus deformation bands. Larger displacement faults affect fluid flow by both the juxtaposition of lithologies with different hydrologic properties and the structural and diagenetic modification of fluid pathways within the fault zone. Small-displacement faults, which are typically not mapped but are common in tectonically active areas [e.g., *Carter and Winter*, 1995], impact fluid flow only by the latter process. These faults are the focus of this paper, in which we report on the inferred effects of deformation bands on vadose zone (above the water table) flow and transport in ignimbrites.

[4] Deformation bands are narrow, tabular fault zones in which grain size reduction, grain boundary sliding, and pore

[1]Department of Geological Sciences, University of Texas at Austin, Austin, Texas, USA.
[2]Department of Geology and Geophysics, University of Wisconsin–Madison, Madison, Wisconsin, USA.
[3]Los Alamos National Laboratory, Los Alamos, New Mexico, USA.

Copyright 2006 by the American Geophysical Union.
0148-0227/06/2005JB003892$09.00

14670

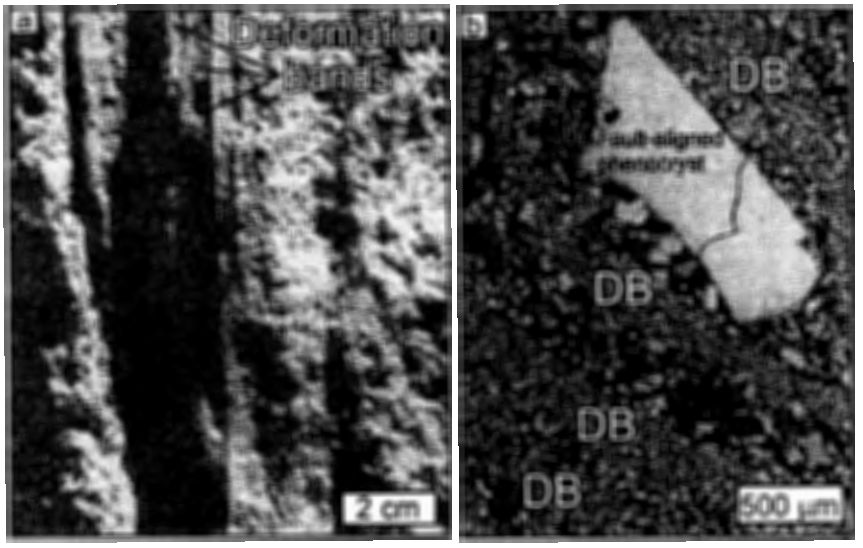

Figure 1. (a) Deformation bands in crystallized, nonwelded Bandelier Tuff. (b) BSE image of deformation bands (DBs) in sample from Figure 1a. Deformation bands are characterized by crushed and/or aligned grains (gray) and collapsed pores (black).

collapse accommodate millimeter-centimeter displacements (Figure 1). Experimental deformation of sedimentary rocks reveals that porosity is one of the dominant petrophysical controls on fracture versus deformation band formation in faults [*Dunn et al.*, 1973]. Accordingly, these structures have been described in high-porosity sandstones [e.g., *Aydin and Johnson*, 1978; *Antonellini and Aydin*, 1994], poorly lithified sands [e.g., *Mozley and Goodwin*, 1995; *Cashman and Cashman*, 2000], and nonwelded ignimbrites [*Wilson et al.*, 2003; *Evans and Bradbury*, 2004]. In contrast to fractures, which increase porosity and saturated permeability with respect to protolith, deformation bands reduce these properties [e.g., *Antonellini and Aydin*, 1994; *Sigda et al.*, 1999]. Under unsaturated conditions, however, permeability is a function of the water content of the geologic medium as well as its pore size and connectivity [*Stephens*, 1996]. In the vadose zone of semiarid to arid climates, where small pores retain water more effectively than large pores, low-porosity deformation bands in sand can be up to 6 orders of magnitude more permeable than surrounding protolith [*Sigda and Wilson*, 2003]. Deformation bands can significantly affect fluid flow and diagenesis, as zones of pore collapse and grain crushing increase both capillarity and the surface area for chemical reaction.

[5] The Bandelier Tuff is a sequence of ignimbrite deposits located in northern New Mexico that, for the most part, has been above the water table since deposition [*Purtymun and Johansen*, 1974] (Figure 2a). The water table is ~152 m below the surface in the study area; thus the vadose zone is very thick. *Wilson et al.* [2003] documented deformation bands in more than half of the stratigraphic thickness of the ignimbrite deposits that define the Pajarito Plateau (Figures 2a and 2b). They showed that these fault zones are found only in nonwelded units of the Bandelier Tuff (Figure 2b). As small-displacement faults, deformation bands are common features of the Pajarito Plateau [cf., *Carter and Winter*, 1995; *Wilson et al.*, 2003]. They are associated with extension along the Rio Grande Rift, and increase in density from a background level of fewer than 1 every 20 m to roughly 1 per 1.5 m directly adjacent to the main strands of the Pajarito fault system [*Riley et al.*, 2005]. However, because these structures were only recently recognized in the area, little is known about their influence on vadose zone fluid flow and transport. *Wilson et al.* [2003] do, however, note that these faults have experienced a different diagenetic history than surrounding protolith.

[6] Modification of deformation bands through diagenesis includes preferential smectite enrichment and calcite cementation. Addition of these minerals to faults in an igneous protolith requires fluid/fault interaction. In this paper, we identify and explore two potential explanations for this interaction: (1) fault zones preferentially retain water and/or (2) fault zones experienced higher fluid flux than protolith. The second of these hypotheses requires the first to be true; that is, vadose zone flow occurs preferentially through already wet pores. The analyses presented here collectively provide evidence of enhanced fluid flow rather than simply preferential water retention within deformation band fault zones. Where sufficiently closely spaced, such faults might therefore accelerate both recharge and contaminant transport through the vadose zone. This study thus enhances our understanding of the record of paleoflow in the Bandelier Tuff and represents a first step toward understanding how deformation bands might affect present-day vadose zone fluid flow and solute transport in this and similar areas.

2. Geologic Setting

[7] Bandelier Tuff ignimbrite deposits are located on the flanks of the Jemez Mountains of northern New Mexico

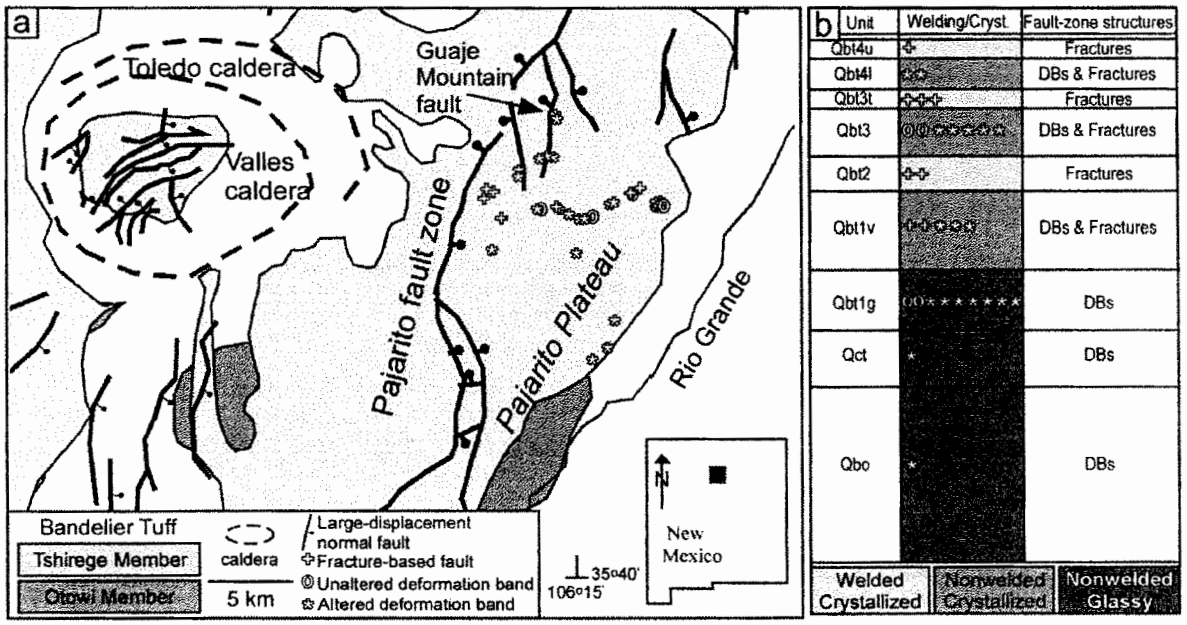

Figure 2. (a) Location map and simplified structure map of the Jemez Mountains modified from *Aldrich* [1986], *Heiken et al.* [1990], and *Purtymun* [1995]. Symbols show locations of different fault types studied on the Pajarito Plateau, the region of Bandelier Tuff exposure east of the Pajarito fault zone. (b) Mechanical stratigraphy of the Bandelier Tuff. Cooling unit stratigraphy is modified from *Lewis et al.* [2002]. Symbols each represent a single location at which outcrop characterization of at least one fault zone was conducted; the dominant type of fault zone is indicated (see legend). DB, deformation band; Qbo, Otowi Member; Qbt, Tshirege Member.

(Figure 2). The ignimbrite sequence consists of the 1.6 Ma Otowi Member (Qbo) and the 1.2 Ma Tshirege Member (Qbt), which were deposited from pyroclastic eruptions of the Valles/Toledo caldera complex [*Smith and Bailey*, 1966; *Izett and Obradovich*, 1994]. Both members are dominated by silicic ash, with subordinate pumice, lithic clasts, and phenocrysts of quartz, sanidine, and plagioclase feldspar [*Broxton et al.*, 1995; *Stimac et al.*, 1996; *Wilson et al.*, 2003].

[8] Ignimbrite deposits locally may be modified during cooling. Bandelier Tuff deposits are composed dominantly of silicic glass [*Stimac et al.*, 1996]. Where this silicic glass has undergone postdepositional devitrification, it is replaced by fine-grained cristobalite and potassium feldspar. During subsequent vapor phase crystallization, silicic glass and vapor-filled pores may be replaced by coarser-grained tridymite, potassium feldspar, minor amounts of cristobalite, and a variety of trace minerals. The latter include micron-scale mineral coatings of magnetite, zircon, titanite (sphene), monazite, apatite, sylvite, barite, chevkinite, and other minerals rich in Ba, Nb, Y, Pb, Bi, Fe, Ag, Cu, Zn, V, Ni, W, and Sn [*Stimac et al.*, 1996]. Vapor can also escape the system through subvertical, roughly tabular elutriation pipes, resulting in the removal of fine-grained matrix [*Freundt et al.*, 2000]. The pipes therefore consist of phenocrysts and lithic fragments. They can be distinguished from faults not only because the pipe-filling material is coarser grained than the matrix, but also because the structures themselves vary abruptly in thickness (from millimeters to centimeters) along both strike and dip and are bound by curviplanar surfaces. *Wilson* [2004] discusses the geochemistry, mineralogy, and saturated permeability of elutriation pipes.

[9] The Otowi Member of the Bandelier Tuff is a single, glassy, nonwelded cooling unit. The Tshirege Member comprises a sequence of cooling units, which vary in degree of welding and postdepositional crystallization (Figure 2b). This variation in postdepositional processes leads to a trace element geochemical stratigraphy [*Stimac et al.*, 1996] as well as a mechanical stratigraphy in which welded units deform by fracture, glassy nonwelded units deform by cataclasis within deformation bands, and crystallized nonwelded units deform by either of these processes (Figure 2b) [*Wilson et al.*, 2003].

[10] On the Pajarito Plateau, the focus of our study, the Bandelier Tuff is cut by the Pajarito fault system, a 41-km-long, rift-related, normal fault system consisting of four large faults, each dipping steeply west or east and striking approximately north (Figure 2a). Displacement is characteristically dip slip, up to 200 m on the Pajarito fault, with local evidence of strike slip [*Gardner and House*, 1987; *Carter and Gardner*, 1995]. Small-displacement (millimeter-meter throw) faults are much more common than these large-displacement faults [e.g., *Carter and Winter*, 1995; *Wilson et al.*, 2003; *Riley et al.*, 2005]. We have focused on these numerous, small-displacement faults, particularly deformation bands in nonwelded ignimbrite

units, which typically exhibit variable diagenetic changes with respect to protolith.

3. Methods

3.1. Outcrop Characterization, Petrography, and Microprobe Analyses

[11] Field characterization of more than 100 small-displacement fault zones in the Bandelier Tuff was conducted over an area covering much of the Pajarito Plateau (Figure 2). Each was identified as either a fracture-based fault or deformation band. Since fractures have been studied extensively on the Pajarito Plateau [e.g., *Wohletz*, 1996; *Vaniman et al.*, 2002], we focus here on deformation band faults. More than two thirds of the deformation band faults identified contain visible clay and/or calcite—minerals that are present only in trace amounts, if at all, in the protolith. A representative subset of nine deformation band faults was chosen for detailed petrographic and microprobe analyses (auxiliary material Table S1).[1] These analyses were conducted to evaluate microstructural evidence of diagenetic processes and obtain data to determine whether clay could be produced solely by reaction of protolith with fluids. The subset of faults analyzed includes three classes of deformation bands, found in both glassy and crystallized nonwelded ignimbrites: (1) low clay content ($\leq$10 wt %), (2) high clay content (>10 wt %), and (3) clay with variable amounts of calcite. Thin sections were prepared from oriented samples of fault zone material and corresponding unaltered protolith. Mineralogy, protolith textures, and fault zone microstructures were analyzed with a petrographic microscope.

[12] Backscattered electron (BSE) imaging and quantitative chemical analysis of protolith matrix and mafic minerals as well as fault zone clay were performed at the New Mexico Bureau of Geology and Mineral Resources on a Cameca SX-100 electron microprobe operated at 15 keV and 20 nA beam current. Pixel counts (1024 × 768 resolution) of black (porosity) versus gray (mineral grain) area in 100 BSE images per protolith thin section (three thin sections per sample) were used to quantify two-dimensional porosity (reported in Tables S2 and S3). Secondary electron (SE) images of freshly broken fault zone and protolith samples were used to document the three-dimensional character of pore spaces and to define the morphology of key diagenetic minerals. Calcite cathodoluminescence was observed with a MAAS/Nuclide Luminiscope, ELM-3R series at <100 mtorr vacuum, 0.3–0.5 mA beam current, and 5–10 kV.

3.2. Bulk Mineralogy (XRD)

[13] The bulk mineralogy of fault zone material and corresponding unaltered protolith was determined by quantitative X-ray diffraction (XRD) analysis. These analyses are critical to quantifying mineralogic changes associated with diagenesis, and evaluating whether those changes require addition of material (other than fluids) to the fault zones. Eight of the nine previously mentioned protolith fault sets were selected for mineralogic analysis (Table S1). Each sample was prepared by crushing in a tungsten carbide shatterbox for approximately 15 min. A small portion of each sample (~0.8 g) was mixed with 1.0-mg corundum (Al_2O_3) internal standard in the ratio of 80% sample to 20% corundum by weight. Each sample was then ground with acetone in an automatic Retsch Micro-Rapid mill (fitted with an agate mortar and pestle) for at least 10 min. This produced a sample with an average particle size of less than 5 μm and ensured thorough mixing of sample and internal standard [*Chipera and Bish*, 2002]. All diffraction patterns were obtained by XRD lab manager S. J. Chipera at Los Alamos National Laboratory on a Siemens D500 X-ray powder diffractometer using CuK (alpha) radiation, incident and diffracted beam Soller slits, and a Kevex Si (Li) solid-state detector from 2° to 70° two-theta, using 0.02 step, and counting for at least 2 s/step. Analysis of each diffraction pattern was conducted using FULLPAT QXRD software [*Chipera and Bish*, 2002]. FULLPAT is a quantitative X-ray diffraction method that merges the advantages of existing full pattern fitting methods with the traditional reference intensity ratio (RIR) method. Like the Rietveld quantitative analysis method, it uses complete diffraction patterns; however, it also analyzes background, which contains important information about matrix effects and sample composition. For this reason, FULLPAT can explicitly analyze all phases in a sample, including partially ordered, disordered, or amorphous phases such as clay minerals and glasses, which contribute disproportionately to background. Addition of the corundum internal standard to both unknown samples and library standards eliminates instrumental and matrix effects and allows unconstrained analyses to be conducted by scaling and matching of corundum-normalized library patterns to each phase in the sample. FULLPAT analysis of spectra collected at Los Alamos for a range of mineral mixture standards gives an estimated standard uncertainty of ±3.4 wt % at the 95% confidence level [*Chipera and Bish*, 2002]. To evaluate reproducibility, we analyzed two protolith samples collected from a single outcrop. The results are identical within a lower error than reported; the greatest difference is exhibited by the amount of the postdepositional phase trydimite, which we know to be spatially variable (Table S3). Analyses of material taken from the same fault allow an investigation of spatial variability in fault mineralogy. Two deformation bands were targeted for these studies. XRD analyses of these deformation bands are again identical within a lower error than reported, with the notable exception of wt % glass and smectite, which are spatially variable and inversely correlated (Table S2).

3.3. Whole Rock Geochemistry (XRF and INAA)

[14] Chemical data were collected from portions of the same samples prepared for XRD analyses (Table S1) to help evaluate whether chemical changes requiring fluid flux accompanied diagenesis. After crushing, samples were prepared for X-ray fluorescence (XRF) analyses following the methods described by *Hallet and Kyle* [1993]. All samples were analyzed by New Mexico Bureau of Geology and Mineral Resources X-ray facility manager C. McKee with a Phillips Panalytical PW2400 wavelength dispersive, sequential X-ray fluorescence spectrometer. An end window Rh tube was used to excite the sample, and fluorescent X rays were detected using a variety of analyzing crystals. All major element data were collected using a tube voltage

[1]Auxiliary material is available at ftp://ftp.agu.org/apend/jb/2005jb003892.

of 35 kV and 75 mA and all trace element concentrations were obtained using an X-ray tube setting of 60 kV and 45 mA. Phillips software was used to control the spectrometer and reduce the raw data. Analytical precision for each major and trace element analysis was calculated according to *Hallet and Kyle* [1993] and is reported as standard deviation in Tables S2 and S3. Replicate analyses performed for several samples, including fault and protolith, demonstrate exceptional reproducibility (Table S4).

[15] Of the eight protolith fault sets analyzed for mineralogy, major oxides, and trace elements, three fault samples containing 36.5–93.5% clay were selected for determination of rare earth element (REE) concentrations by instrumental neutron activation analysis (INAA) (Table S1; data in Tables S2 and S3). The analyses were conducted to allow us to evaluate clay source. Specifically, clay produced solely by alteration of protolith should have REE profiles similar to protolith; externally sourced clay would exhibit different patterns.

[16] Samples were prepared for INAA by sample disruption with a sonic probe, sequential sedimentation in deionized water, and centrifugation at 8000 rpm. Separates were then allowed to dry in order to evaporate the centrifuged supernatant to obtain purified clay as a <0.1 μm size fraction. These clay separates were analyzed in the trace element geochemistry laboratory at Washington University–St. Louis by R. Korotev using methods described by *Korotev* [1991].

3.4. Stable Isotope Characterization

[17] Stable isotope analyses of samples from three deformation band fault zones were conducted to evaluate both the extent of fluid-rock interaction and potential fluid sources. Sample sets were chosen from the eight faults for which outcrop, petrographic, microprobe, XRD, and XRF analyses were performed (Table S1). The three sample sets include the full variety of deformation band fault types mentioned previously. Samples of fault material, footwall and hanging wall rock material <5 mm from the fault boundaries, and corresponding protolith (>50 cm from fault boundaries) were prepared for isotope analysis by manual grinding using a mortar and pestle and subsequently sieved to <1 mm grain size. Silicate samples were reacted with chlorine trifluoride (ClF_3) reagent at elevated temperature to liberate molecular oxygen [cf. *Campbell and Larsen*, 1998]. A subsequent reaction with a hot carbon rod converted the evolved oxygen to CO_2 gas, which was then analyzed with a Finnigan MAT Delta E isotope ratio mass spectrometer. One calcite-cemented fault sample was reacted with 100% phosphoric acid [*McCrea*, 1950], and the evolved CO_2 gas analyzed for carbon and oxygen isotopic composition on the mass spectrometer. All samples were analyzed by A. Campbell in the Stable Isotope Mass Spectrometry Laboratory at the New Mexico Institute of Mining and Technology.

4. Results

4.1. Outcrop Character and Petrography of Protolith-Deformation Band Sets

[18] All of the Bandelier Tuff cooling units that fail through the formation of deformation bands are nonwelded, but they may be either glassy or crystallized [*Wilson et al.*, 2003]. The latter units are characterized by greater resistance to weathering and "punky" appearance of pumice clasts in outcrop. Because of the variations in postdepositional crystallization reviewed earlier, the ignimbrites range in color from white to lavender to orange. Each unit is dominated by variably crystallized silicic ash (2-μm- to 2-mm-sized grains), with subordinate millimeter-sized phenocrysts and centimeter-scale pumice and lithic clasts. Thus the undeformed ignimbrite units have a wide grain size distribution, ranging from clay-sized particles to centimeter-scale grains. On the basis of qualitative observations in thin section, there are roughly equal volumes of centimeter-scale and millimeter-scale fragments in the undeformed Bandelier Tuff.

[19] Deformation bands that lack diagenetic phases are composed of grain-size-reduced glass shards, pumice fragments, lithic clasts, and phenocrysts (Figure 1) [*Wilson et al.*, 2003], making them slightly lighter in color and more resistant to weathering than protolith. Deformation bands also have a wide grain size distribution, but the majority of grains are relatively small. Commonly, glass and pumice fragments make up the smallest grains, and the few remaining larger grains are mechanically stronger phenocrysts and lithic clasts. These stronger grains are typically aligned with long axes subparallel to deformation band boundaries. Locally, phenocrysts are bypassed completely by individual deformation bands (Figure 1b). The stronger grains are not typically crushed, but do contain microfractures that are probably the result of thermal contraction upon rapid cooling during deposition rather than fault zone deformation [cf. *Sommer*, 1977; *Wallace et al.*, 1999]. Transgranular fractures are not preserved in deformation bands.

[20] Fault zone diagenesis is evidenced by mesoscopically visible modification of the color and character of deformation band faults (Figures 3a, 3b, and 3c). Parts of faults that are enriched in clay are dark orange to brown and commonly exhibit distinct foliation; microcrystalline calcite typically occurs in white, fault-parallel bands that are strongly resistant to weathering and react with dilute HCl. In thin section, it is evident that the majority of clay and calcite is located at the margins of and in the interstices between ignimbrite fragments. Clay is particularly common along glass and mafic grain boundaries, as well as within some pumice vesicles (Figures 3d and 3e).

[21] Clay within deformation bands typically exhibits desiccation cracks (Figure 3f). In thin section, two distinct clay morphologies are evident, depending on its abundance within the fault. In deformation bands with ≤10 wt % clay (Figure 3a), grains are mostly clay-sized and show little or no birefringence or color. In deformation bands with >10 wt % clay, larger grains and books of clay exhibit an orange to brown color with plane-polarized light, and display mottled birds-eye extinction with crossed polars. The distortion and desiccation cracking evident in these clay accumulations is typically associated with wetting and drying cycles.

[22] In many of the deformation bands with little or no evidence of shear displacement subsequent to the introduction of clay, clay lines pores and fills matrix porosity (Figure 3d). Another clay texture that is less common (or less commonly preserved) is one in which glass shards appear to have altered to clay (Figure 3e). We infer that these diagenetic microstructures were destroyed where

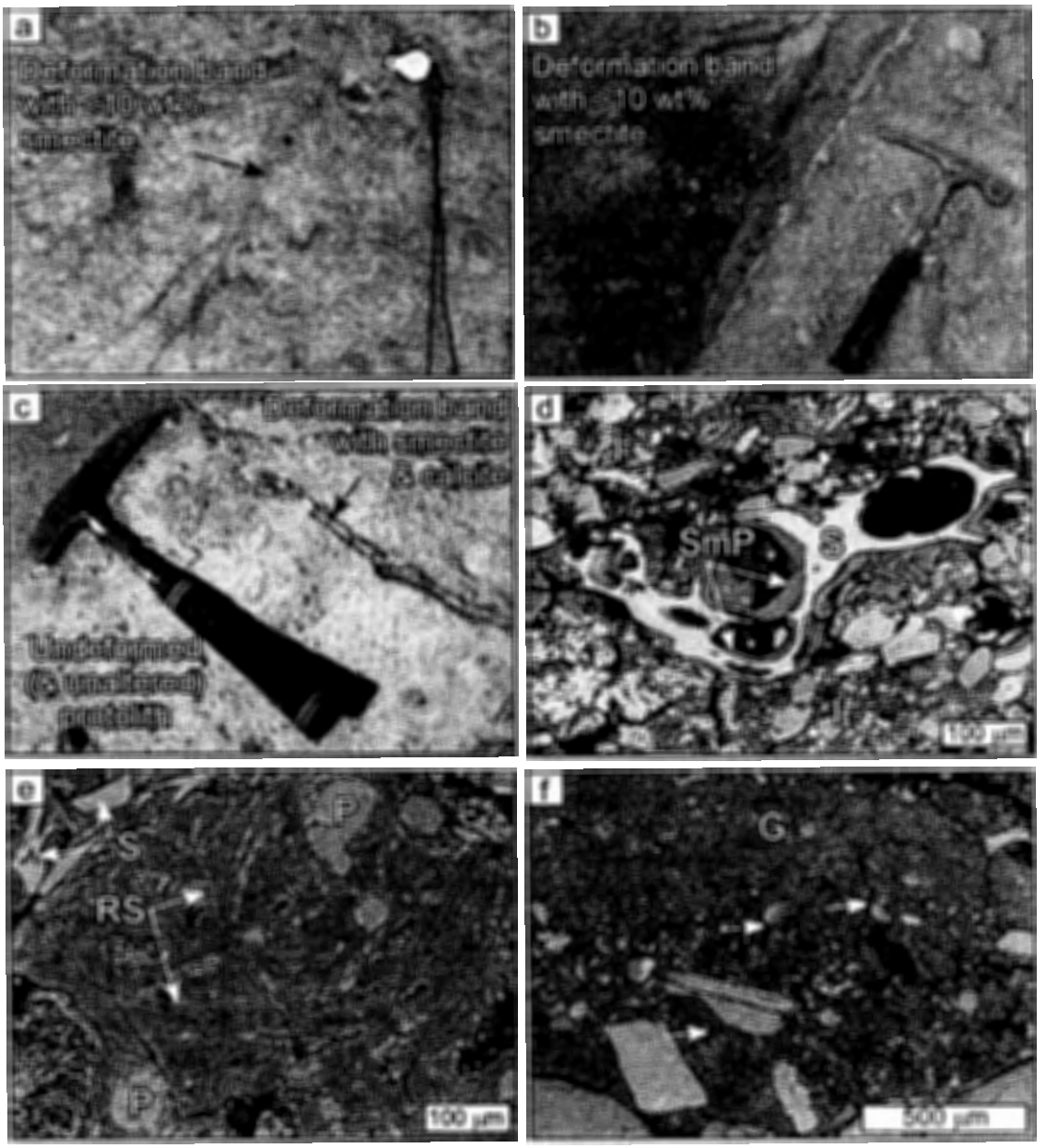

Figure 3. Outcrop photos of deformation bands with (a) $\leq$10 wt % clay, (b) >10 wt % clay, and (c) >10 wt % clay and calcite. Figures 3d, 3e, and 3f are BSE images of deformation bands with >10 wt % clay. BSE images are from deformation bands other than those shown in Figures 3a, 3b, and 3c. (d) Microstructures similar to those of translocated (eluviated) clay seen in soils. SmP, smectite-lined pore; S, glass shard; I, grain-size-reduced ignimbrite. Note the diffuse boundary between glass and clay, suggesting post-translocation, in situ alteration. (e) Microstructural evidence of glass shards (margins outlined with dashed lines for clarity) that have altered to clay. S, glass shard; RS, relict glass shard; P, phenocryst. (f) Compositional banding foliation (G) and clast alignment developed by shear in a clay-rich deformation band. Only deformation band (no protolith) is shown in image. Arrows show representative desiccation cracks in clay.

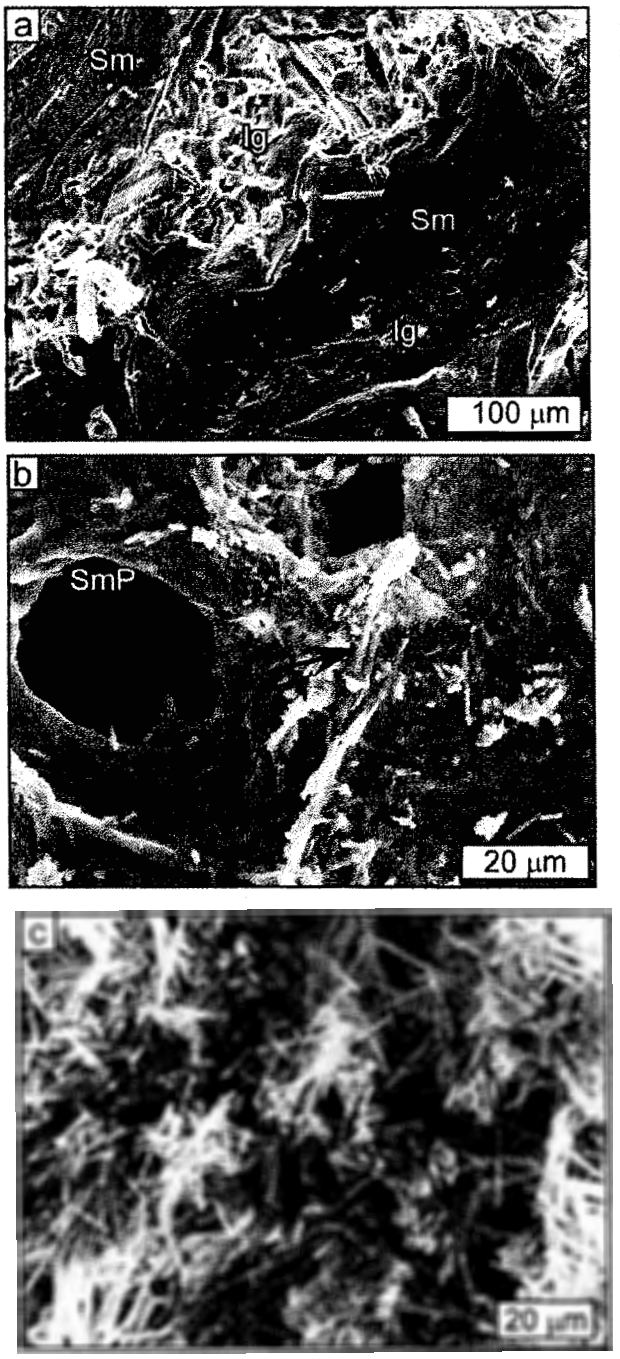

Figure 4. SE images of (a) compositional-banding foliation of smectite (Sm) and ignimbrite material (Ig) in a deformation band (bt7) containing 70.2 wt % clay, (b) smectite-lined pores (SmP) in a deformation band (bt111b) containing 36.5 wt % clay and 3 wt % calcite (representative microcrystallites shown by arrows), and (c) calcite microcrystallites within a calcite-cemented deformation band (bt66).

deformation bands were reactivated, resulting in clast alignment and the formation of compositional-banding foliation (Figure 3f). Compositional bands are composed of variable amounts of foliated clay and fragments of ignimbrite and clay (Figure 4a).

[23] Clay is always present in calcite-cemented deformation bands. Calcite segregations are situated in the middle of the fault (Figure 3c), at the fault boundary, or as lenses within the clay. White, cohesive, calcite-cemented layers typically define a compositional banding foliation with clay (Figure 3c). Both ignimbrite and clay fragments are common in the calcite layers. Also, many of these deformation bands contain plant roots that extend several meters into the subsurface. In some places, calcite is concentrated along these roots.

[24] Calcite in deformation bands of the Bandelier Tuff is not a pure, coarsely crystalline, void-filling mineral. Instead, secondary electron (SE) images reveal that it consists of rod-shaped microcrystallites (needle-fiber calcite of *Verrecchia and Verrecchia* [1994]) (Figures 4b and 4c). Common calcite morphologies in these deformation band faults fall into two categories: (1) single or coupled smooth rods 1–2 μm wide and 5–20 μm long and (2) serrate rods 5 μm wide and 100 μm long. Calcite is nonluminescent.

4.2. Mineralogy and Whole Rock Geochemistry of Protolith-Deformation Band Sets

[25] Bulk mineralogy, major oxide, and trace element geochemical data for eight protolith fault sets are given in Tables S2 and S3. As mentioned previously, ignimbrite deposits are inherently heterogeneous. This heterogeneity is evident in the variability in mineralogy and chemistry of protolith analyzed for this and previous studies (Figures 5, 6, and 7). In this section and later discussion, we focus on bulk differences between deformation band and protolith mineralogy and chemical signatures that are not only greater than protolith variation (including variation documented far from the faults we have analyzed), but also greater than detection limits, analytical errors, and estimated precision (given in Tables S2 and S3).

[26] Each protolith unit contains significant quartz, alkali feldspar, and plagioclase feldspar with minor (commonly less than analytical uncertainty of 3.4 wt %) hematite ± magnetite ± augite ± biotite (Figures 5a, 6a, and 7a). Glassy units are dominated by silicic glass and lack cristobalite and tridymite, whereas crystallized units contain higher amounts of cristobalite and tridymite than glass. Deformation bands include these phases as well as the diagenetic clay and calcite discussed in precious sections. XRD analyses demonstrate that the clay is a highly disordered smectite (a general term for montmorillonite group minerals) (S. J. Chipera, personal communication, 2006). The disorder is reflected in a broad, asymmetric (001) peak that is best matched by a library standard of smectite from local soil. Microprobe analyses discussed in a following section show that this fault zone clay is high in Mg and Fe and low in K, as would be expected of smectite (Table S6). We did not analyze a clay separate to determine exactly what clay minerals are represented in this disordered system, so will use only the general term "smectite" for the remainder of the paper.

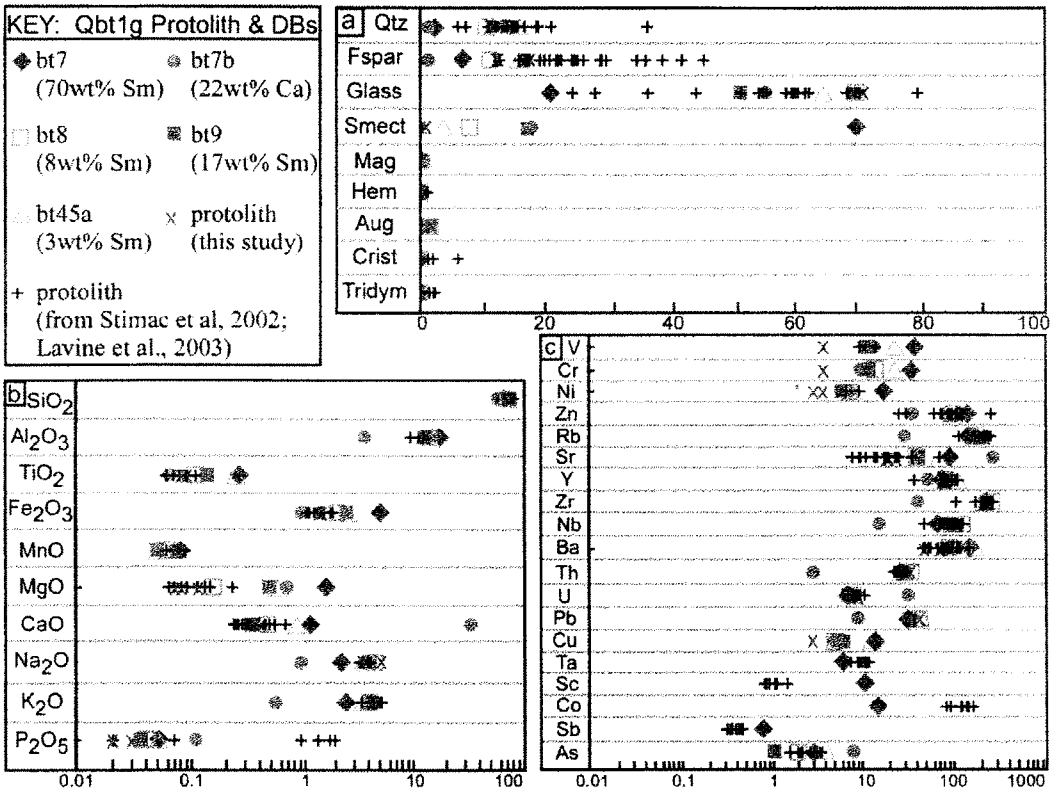

Figure 5. (a) Mineralogy (except for calcite, which is present only in bt7b), (b) major oxide abundances, and (c) trace element concentrations of deformation bands and adjacent protolith for glassy nonwelded Qbt1g (compare Figure 2b). Mineralogy and major oxide abundances are given in wt %; trace element concentrations are given in ppm. Detailed data from this study are given in Tables S1 and S2. DB, deformation band; Qtz, quartz; Fspar, plagioclase and alkali feldspar; Smect, smectite; Mag, magnetite; Hem, hematite; Aug, augite; Crist, cristobalite; Tridym, tridymite.

[27] Differences in diagenetic mineral content between protolith and faults are marked. Glassy Qbt1g protolith contains 0–2.2 wt % smectite and no detectable calcite. Associated deformation bands include 2.7–70.2 wt % smectite and 0–21.7 wt % calcite. Crystallized Qbt3 and Qb4 protolith have no detectable smectite or calcite. Associated deformation bands contain 0–93.5 wt % smectite and 0–2.8 wt % calcite. We note that amounts of these phases are locally less than the analytical uncertainty of 3.4 wt %. Thus, although the minerals are demonstrably present (producing measurable peaks in XRD spectra), they may be present in slightly smaller or larger amounts than indicated.

[28] Deformation bands show variable differences in bulk mineralogy and abundances of major, minor, and trace elements relative to adjacent protolith (Table 1 and Figures 5, 6, and 7). In general, faults with a larger percentage of diagenetic minerals exhibit greater differences in chemistry relative to protolith. In the following paragraphs, we offer a conservative analysis of these differences. Because addition of smectite and calcite increases the volatile content of deformation bands, and therefore measured loss on ignition (LOI), we have normalized major element analyses to 0% LOI, which minimizes differences between fault zones and protolith (compare LOI in fault with no diagenetic phases to one with smectite and calcite in Table S4). In addition, we utilize previous analyses of protolith in order to consider the full range of variability demonstrated by these heterogeneous units. We also consider whether any species in the system are appropriately deemed conservative. Our microstructural observations suggest that deformation bands may skirt stronger quartz and feldspar phenocrysts (e.g., Figure 2a), thereby preferentially sampling glass. In addition, the textures of undeformed clay present in some deformation bands (e.g., Figure 3d) suggest it may have been deposited in pores. Addition of clay, rather than in situ production, would add material to the fault zone. Notably, it would add TiO_2 and Al_2O_3, which would normally be considered immobile elements. In other words, the physical processes recorded by these fault zones preclude a more sophisticated analysis (such as that suggested by *Gresens* [1967] and *Grant* [1986]) than that offered, as we cannot demonstrate immobility of a single species in this system. As a simple illustration of the magnitude of the differences we document, we have highlighted variations of 100% or greater in bold in Table 1.

[29] A deformation band (bt116) with 1.4 wt % smectite in crystallized nonwelded unit Qbt3 is geochemically indis-

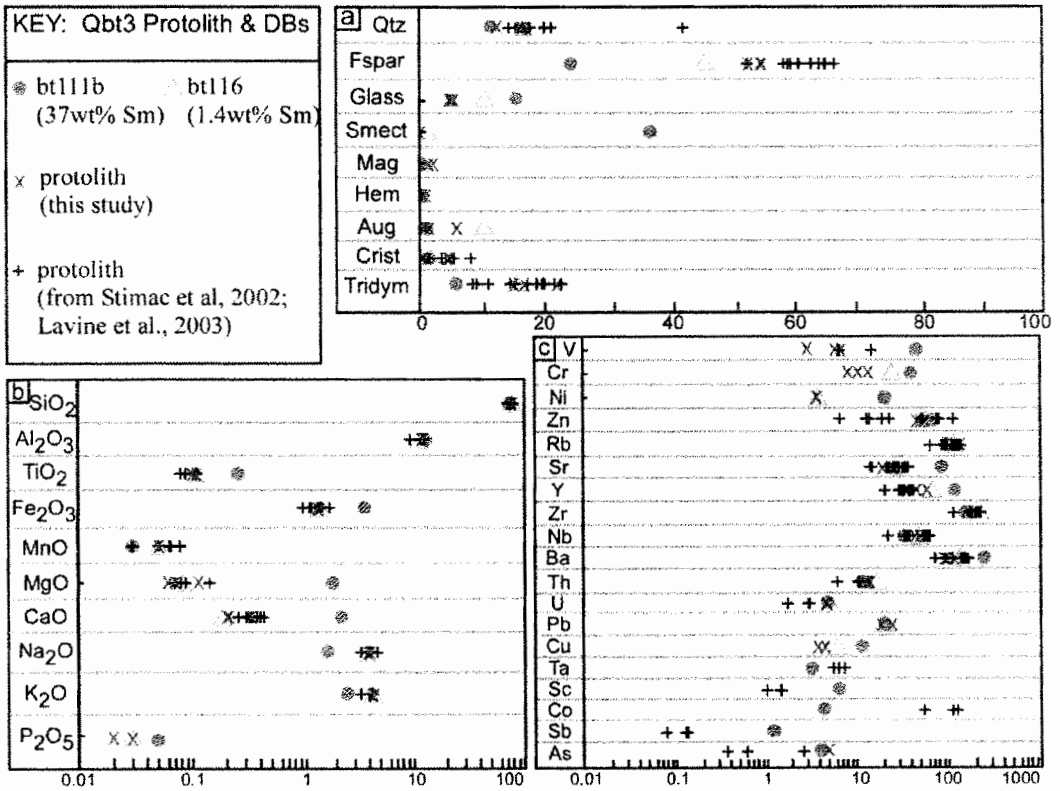

Figure 6. (a) Mineralogy (except for calcite, which is only present in bt111b), (b) major oxide abundances, and (c) trace element concentrations of deformation bands and adjacent protolith for crystallized nonwelded Qbt3 (compare Figure 2b). Mineralogy and major oxide abundances are given in wt %; trace element concentrations are given in ppm. Detailed data from this study are given in Tables S1 and S3. Abbreviations are as given in Figure 5 caption.

tinguishable from protolith (Figure 6a). Deformation bands bt45a and bt8 in glassy nonwelded unit Qbt1g have 2.7 and 10.4 (average) wt % smectite respectively. Both faults have more Cu than protolith; bt8 has more smectite and bt45a is also higher in TiO_2, MgO, and Cr (Figure 5).

[30] Deformation band bt119 in crystallized nonwelded unit Qbt4 has 93.4 wt % smectite. In addition to being enriched in clay, it is higher in Al_2O_3, Fe_2O_3, MgO, CaO, V, Cr, Ni, Y, Cu, Sc, Sb, and As than protolith (Figure 7). This deformation band has less feldspar, tridymite, SiO_2, MnO, Na_2O, K_2O, Nb, Ta, and Co than protolith (Figure 7). In glassy nonwelded unit Qbt1g, deformation bands with an average of 22.2 wt % (bt9) and 70.2 wt % (bt7) smectite are higher in smectite, Fe_2O_3, and MgO than protolith; bt7 is also higher in TiO_2, Al_2O_3, V, Cr, Sr, Sc, and Sb and lower in SiO_2, Na_2O, K_2O, and Co than protolith (Figures 5b and 5c and Table 1; note that REEs were not analyzed for bt9).

[31] A deformation band with 36.5 wt % smectite and 2.8% calcite in crystallized nonwelded unit Qbt3 (bt111b) is higher in smectite, calcite, glass, Al_2O_3, TiO_2, Fe_2O_3, MgO, CaO, V, Cr, Ni, Y, Ba, Cu, Sc, and Sb than protolith (Figure 6). This deformation band is lower in feldspar, Na_2O, K_2O, Ta, and Co (Figure 6). In glassy unit Qbt1g, this type of deformation band is represented by bt7b, which has 18.1 wt % smectite and 21.7 wt % calcite (both higher than protolith), and is higher in MgO, CaO, Sr, U, As, and Cu (Figure 5). It has less quartz, SiO_2, Al_2O_3, Na_2O, K_2O, Rb, Zr, Nb, Th, and Pb than protolith (Figure 5 and Table 1).

[32] Some of these variations are easily explained: a deformation band with less quartz than protolith will logically have less SiO_2. If smectite were physically added to the fault zone, it could add SiO_2, Al_2O_3, TiO_2, Fe_2O_3, MgO, and CaO as well as adsorbed trace elements, and effectively dilute other elements. Similarly, the addition of calcite would add CaO. We consider these more common trends in the Discussion.

4.3. Chemical Compositions of Protolith Matrix, Mafic Minerals, and Fault Zone Smectite

[33] Chemical analyses of Fe-bearing phases in several protolith-deformation band fault pairs were performed with the electron microprobe (Tables S5 and S6). The fault zones chosen contain 1.4 to 93.5 wt % smectite. These analyses provide the compositions of phases that may have been involved in fluid-fault reactions producing smectite. Comparison of fault and protolith data can help determine whether or not material was added to, or removed from, the fault zones during diagenesis (Table 2).

[34] Fe is relatively scarce in rhyolitic ignimbrite deposits, but is more abundant in fault zone smectites (Tables S2

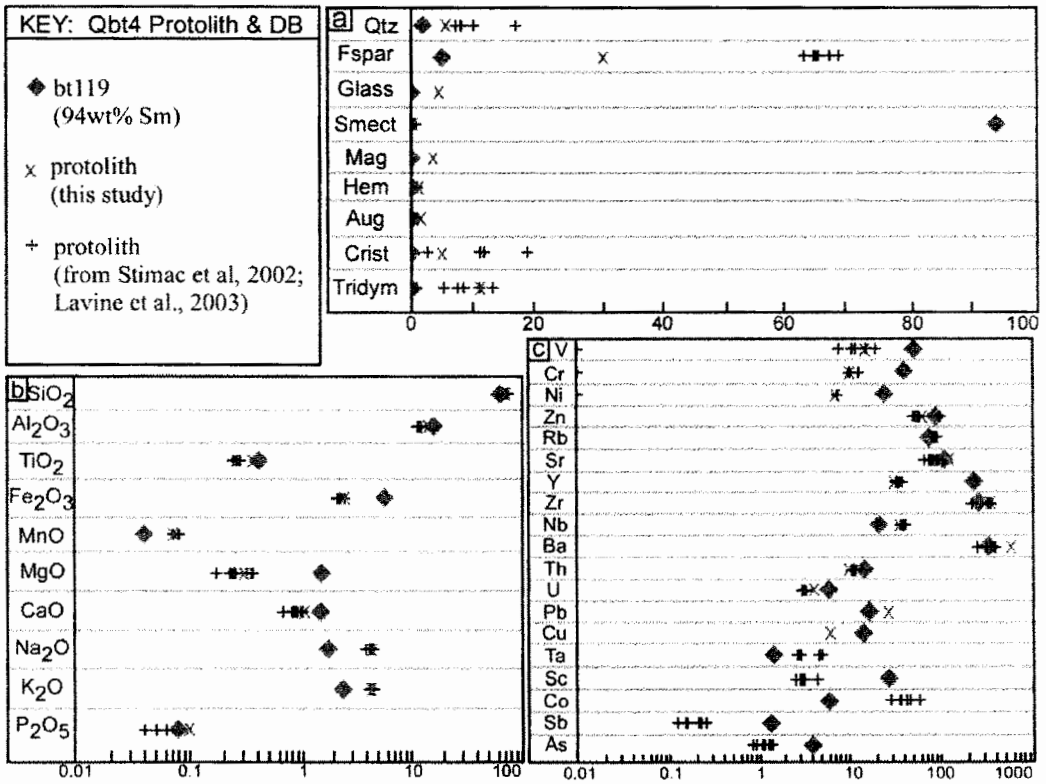

Figure 7. (a) Mineralogy, (b) major oxide abundances, and (c) trace element concentrations of deformation bands and adjacent protolith for crystallized nonwelded Qbt4 (compare Figure 2b). Mineralogy and major oxide abundances are given in wt %; trace element concentrations are given in ppm. Detailed data from this study given in Tables S1 and S3. Abbreviations are as given in Figure 5

and S3). The Fe content of each sample tracks several Fe-bearing phases in the Bandelier Tuff, such as glass, alkali feldspar, augite, magnetite, and smectite. We calculate the total amount of Fe (FeO and Fe_2O_3) available from these phases in a given protolith or fault zone sample (Table 2) by multiplying the wt % abundance of a phase by the average wt % Fe contained within that phase (Tables S5 and S6). The wt % Fe for all phases is then summed for fault and for protolith. This simple mass balance calculation shows that there are variable but small differences in Fe in the faults analyzed relative to protolith (Table 2). Reductions range from 0.1 to 0.3 wt % Fe, and increases range from 0.3 to 1.9 wt % Fe. These differences are small relative to the standard deviation of wt % Fe determined for individual Fe-bearing phases within and outside the faults, which are 0.02 wt % for alkali feldspar, 2.4 wt % for augite, 2.7 wt % for magnetite, and 1.3 wt % for smectite (Tables S5 and S6).

4.4. Rare Earth Element Distributions of Deformation Bands and Protolith

[35] Rare earth element distributions of fault zone smectite (determined in this study) and corresponding protolith [from *Stimac et al.*, 2002] for each nonwelded Bandelier Tuff unit are given in the chondrite-normalized plots in Figure 8. Data were normalized according to *Nakamura* [1974]. All rare earth element patterns exhibit a negative Eu anomaly and an overall negative slope. Each of the three fault zone smectites analyzed has higher La, Nd, Sm, Eu, and Tb concentrations than associated protolith. In the crystallized nonwelded units (Figures 8b and 8c), the smectite-rich deformation bands also have higher Yb and Lu concentrations than protolith, and exhibit negative Ce anomalies. The fault in glassy nonwelded protolith, however, exhibits only slightly elevated REE values, whereas faults in crystallized units are significantly elevated in every REE but Ce. Despite significant differences in smectite content, the similarities in the latter REE patterns suggest that the smectite was introduced to the fault zones by similar processes.

4.5. Stable Isotope Characterization of Deformation Bands and Adjacent Protolith

[36] Three protolith fault sets were analyzed for stable isotope composition (Table S1). Two of the faults contain smectite, though of quite different amounts; one has smectite and calcite. Protolith (samples >50 cm from fault zone boundary) silicate $\delta^{18}O$ analyses range from 6.1 to 6.8‰ (Table 3), values that are typical of igneous rocks and fluids [*Campbell and Larsen*, 1998]. In the fault zones analyzed, $\delta^{18}O$ values are higher than those of protolith, especially at the fault zone margins (<5 mm from fault zone; Figure 9). Analysis of one calcite-cemented deformation band similar

Table 1. Minerologic and Geochemical Differences Between Deformation Band Types and Adjacent Protolith[a]

Deformation Band Type	Samples	Mineralogy	Major Oxides	Trace Elements
DB with ≤10 wt % smectite				
Crystallized protolith (Qbt3)	bt116/bt116b	none	none	none
1 fault/protolith set analyzed				
Glassy protolith (Qbt1g)	bt45a/bt45c, bt8/bt8/9b	nc/+ Smect	+/nc **TiO_2**, +/nc **MgO**	+/nc **Cr**, +**Cu**
Two fault/protolith sets analyzed				
DB with >10 wt % smectite				
Crystallized protolith (Qbt4)	bt119/bt120	+Smect, −Qtz, −**Feld**, −**Trid**	+**Fe_2O_3**, +**MgO**, +Al_2O_3, +CaO	+V, +Cr, +Ni, +Y, +As,
One fault/protolith set analyzed			−SiO_2, −MnO, −Na_2O, −K_2O	+Cu, +Sc, +Sb, −Nb, −Ta, −Co
Glassy protolith (Qbt1g)	bt9/bt8/9b, bt7/bt7c	+**Smect**, nc/−Qtz, nc/−Feld	nc/+ **TiO_2**, nc/+ Al_2O_3, +**Fe_2O_3**, +**MgO**	nc/+ **V**, nc/+ **Cr**, nc/+Sr, NA/+Ta,
Two fault/protolith sets analyzed			+CaO, −SiO_2, nc/−Na_2O, nc/−K_2O	NA/+ Sb, NA/+Sc, NA/−Co
DB with >10 wt % smectite + calcite				
Crystallized protolith (Qbt3)	bt111b/bt68	+**Smect**, +**Calc**, +**Glass**	+**TiO_2**, +**Fe_2O_3**, +**MgO**, +**CaO**, +Al_2O_3	+V, +Cr, +Ni, +Y, +Ba,
One fault/protolith set analyzed		−Feld	−SiO_2, −Na_2O, −K_2O	+Cu, +Sc, +Sb, −Ta, −Co
Glassy protolith (Qbt1g)	bt7b/bt7c	+**Smect**, +**Calc**	+**MgO**, +**CaO**, −Al_2O_3, −Fe_2O_3,	+**Sr**, +**U**, +**As**, +Cu
One fault/protolith set analyzed		−Qtz, −Feld	−SiO_2, −Na_2O, −K_2O	−Rb, −Zr, −Nb, −Th, −Pb

[a]Qtz, quartz; Smect, smectite; Feld, alkali and plagioclase feldspar; Calc, calcite; Trid, tridymite. DB indicates deformation band type. NA and nc indicate that minerals or elements were not analyzed or show no change in one of the examples listed. Variations of 100% or more are bold. Positive entries are minerals or elements in which deformation band is high relative to protolith, negative entries are minerals or elements in which deformation band is relatively low.

to that shown in Figure 6 gives a $\delta^{13}C$ value of −9‰ and a $\delta^{18}O$ value of 20.8‰.

5. Discussion

[37] We began this paper by stating two hypotheses to explain deformation band fault diagenesis in the Bandelier Tuff: (1) preferential fluid retention in deformation bands relative to protolith due to smaller pore size and (2) preferential fluid flux in faults. The first would result in in situ alteration of grain-size-reduced tuff in faults; the second would additionally leave a record of material preferentially added to the fault zone. In the following sections, we discuss how the different lines of evidence we have presented allow us to evaluate whether the first or both hypotheses are correct.

5.1. Origin of Smectite in Deformation Bands

[38] Microstructural, geochemical, and mineralogical evidence record two different mechanisms by which deformation band fault zones have been enriched in smectite: in situ alteration and translocation. Localized in situ alteration is evidenced by smectite surrounding some shards (glassy or devitrified) and mafic lithic fragments that exhibit very diffuse grain boundaries. In these cases, smectite appears to be replacing the glass and mafic grains (e.g., Figure 3e). This is consistent with the REE pattern of fault zone smectite from a deformation band in glassy nonwelded Qbt1g (Figure 8a), which is virtually identical to that of protolith. In crystallized nonwelded units Qbt3 and Qbt4, feldspar content decreases with increasing smectite content in deformation bands (Table S3), suggesting that smectite in these deformation bands is produced in part by alteration of feldspar grains. In faults where we analyzed two samples to explore spatial variations in fault zone mineralogy (bt8a,b and bt9a,b), there is an inverse relationship between glass and smectite content, reinforcing the inference from microstructural observations that smectite is forming in part through alteration of glass.

[39] Fault zone smectite also coats unaltered grains and locally both lines and fills pores, textures similar to those found in Bt (clay-rich) horizons of desert soils (Figure 3d) [cf. *Davenport et al.*, 1995; *Gile et al.*, 1995; *Vaniman and Chipera*, 1995]. The latter microstructures suggest the introduction of smectite by transport from an external source (translocation), likely in colloidal form. Rare earth element signatures of fault zone smectites observed in crystallized nonwelded Qbt3 and Qbt4 (Figures 8b and 8c) are similar to those of soil-derived smectites analyzed by *Vaniman et al.* [2002]. Both have elevated REE patterns relative to protolith, a pronounced negative Ce anomaly, and a Eu anomaly that is similar to that of protolith. This interpretation is consistent with XRD analyses, which show that clay peaks are best matched by highly disordered, local soil smectite.

[40] We therefore propose that both in situ alteration of protolith matrix and translocation of smectite are responsible for clay concentrations in deformation band faults. The extent to which one process dominates over the other is unclear, and may vary with location or protolith. For deformation bands in which the amount of smectite exceeds the porosity of the unaltered rock (i.e., the space that can be filled with translocated clay, e.g., Figure 8a), in situ alteration must be a significant process of smectite production.

Table 2. Mass Balance Calculations of Total Fe ($FeO + Fe_2O_3$) in Fe-Bearing Phases of Protolith-Deformation Band Pairs[a]

Phase	Weight Percent Phase		Weight Percent Fe in Phase[c]	Calculated Fe, wt %		Difference in Weight Percent Fe[e]
	Protolith[b]	Fault[b]		Protolith[d]	Fault[d]	
			Protolith/Fault Sample: bt116b/bt116			
Glass	4.7	9.6	1.3	0.1	0.1	
Alkali feldspar	53.8	45.0	0.3	0.2	0.1	
Magnetite	0.0	0.0	89.7	0.0	0.0	
Augite	6.0	10.4	24.3	1.5	2.5	
Smectite	0.0	1.4	4.6	0.0	0.1	
Totals				1.7	2.9	+1.2
			Protolith/Fault Sample: bt45c/bt45a			
Glass	70.0	64.0	1.3	0.9	0.8	
Alkali feldspar	17.0	16.0	0.3	0.1	0.0	
Magnetite	0.0	0.0	89.7	0.0	0.0	
Augite	2.0	1.0	24.3	0.5	0.2	
Smectite	0.0	3.0	4.6	0.0	0.1	
Totals				1.4	1.3	−0.1
			Protolith/Fault Sample: bt8/9b/bt9			
Glass	69.3	50.5	1.3	0.9	0.7	
Alkali feldspar	12.5	16.2	0.3	0.0	0.0	
Magnetite	0.0	0.1	89.7	0.0	0.1	
Augite	2.4	1.3	24.3	0.6	0.3	
Smectite	2.2	17.4	4.6	0.1	0.8	
Totals				1.6	1.9	+ 0.3
			Protolith/Fault Sample: bt68/bt111b			
Glass	4.0	16.0	1.3	0.1	0.2	
Alkali feldspar	55.1	24.1	0.3	0.2	0.1	
Magnetite	2.3	0.0	89.7	2.1	0.0	
Augite	1.2	1.2	24.3	0.3	0.3	
Smectite	0.0	36.5	4.6	0.0	1.7	
Totals				2.6	2.3	−0.3
			Protolith/Fault Sample: bt7c/bt7			
Glass	71.9	21.2	1.3	0.9	0.3	
Alkali feldspar	13.0	6.6	0.3	0.0	0.0	
Magnetite	0.1	0.0	89.7	0.1	0.0	
Augite	1.9	0.0	24.3	0.5	0.0	
Smectite	1.5	70.2	4.6	0.1	3.2	
Totals				1.6	3.5	+1.9
			Protolith/Fault Sample: bt120/bt119			
Glass	4.2	0.0	1.3	0.1	0.0	
Alkali feldspar	29.9	4.8	0.3	0.1	0.0	
Magnetite	4.2	0.0	89.7	3.8	0.0	
Pyroxene	1.6	0.0	24.3	0.4	0.0	
Smectite	0.0	88.8	4.6	0.0	4.1	
Montmorillonite	0.0	4.7	0.8	0.0	0.0	
Totals				4.3	4.1	−0.2

[a]Sample numbers correspond to those given in Table S1.
[b]Determined from XRD analysis. Analytical error is 3.4 wt %.
[c]Total Fe ($FeO + Fe_2O_3$) determined by quantitative chemical analyses of phases using electron microprobe.
[d]Calculated as the product of the wt % phase in sample and the wt % total Fe contributed by that phase divided by 100.
[e]Positive difference (indicated by positive number) indicates an increase in total Fe from protolith to fault.

This occurs in two of the faults analyzed, in which the smectite content is 70.2 wt % and 93.5 wt % of fault material, and unaltered protolith have porosities of 49% and 42%, respectively (Tables S2 and S3). We note the possibility of a positive feedback in these processes of clay enrichment: as pore space is filled with translocated clay, it will hold moisture against the grains it coats, facilitating alteration. In situ alteration of glass, feldspar and mafic minerals to form smectite in these faults requires higher amounts or longer residence times of fluid in the deformation band relative to protolith to facilitate alteration. Translocation of smectite, recorded by both REE signatures and microstructures, requires preferential fluid flow.

5.2. Calcite Cementation in Deformation Bands

[41] Two distinguishing features of calcite-cemented deformation bands are (1) rod-shaped calcite micromorphology (Figure 4c) and (2) high levels of CaO relative to protolith (Figures 5b and 6b). The smooth and serrate rods described earlier are characteristic of calcite precipitation associated with microbial activity in the presence of decaying plant roots and with the physicochemical process of desiccation, respectively, in a pedogenic environment

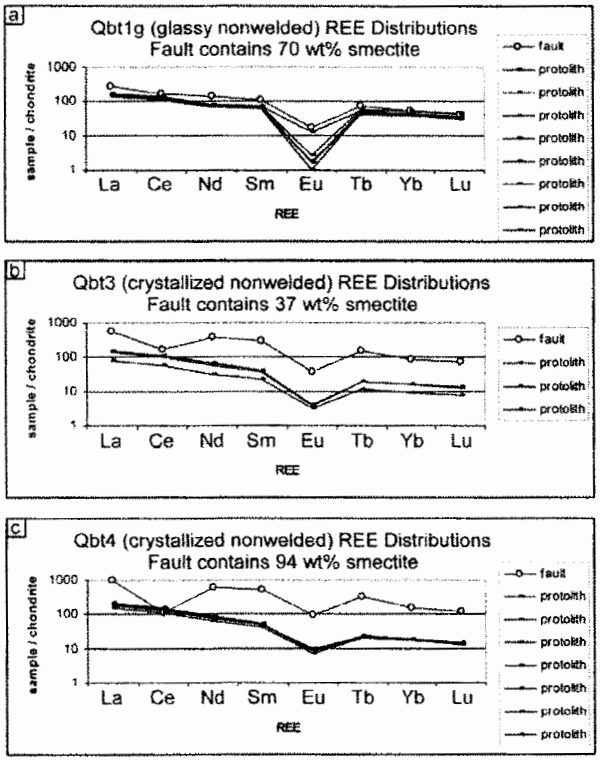

Figure 8. REE distributions for clay-rich (>10 wt % smectite) deformation bands and adjacent protolith, given by Bandelier Tuff unit (compare Figure 2b). Protolith values are from *Stimac et al.* [2002]; fault values are determined in this study. Note the similarity of fault zone smectite patterns in Figures 8b and 8c, both of which are significantly elevated relative to protolith in every element but Ce.

[*Verrecchia and Verrecchia*, 1994]. Desiccation results from long dry spells alternating with brief wet periods, typical of desert environments. During dry periods, evaporation causes supersaturation of solutions and the rapid precipitation of crystals. Inhibition of lateral crystalline growth by adsorbed ions or clays is a common explanation for the acicular shape typical of crystals formed in this way [*Verrecchia and Verrecchia*, 1994]. The spatial association between smectite and calcite in these deformation bands suggests that desiccation of this swelling clay may play a key role in determining the rod-shaped morphology of calcite crystallites. Downward transport of eolian dust by dissolution/precipitation during transient precipitation events can facilitate addition of $CaCO_3$ to deformation bands. Such pedogenic mobilization of eolian dust is the primary mechanism for producing calcic soils in arid environments [*Gile et al.*, 1981; *Quade and Cerling*, 1990], including the Pajarito Plateau [*Eberly et al.*, 1996]. A pedogenic source for the calcite is consistent with the observed nonluminescence of this mineral [cf. *Monger and Adams*, 1996].

[42] Widespread observations of preferential root growth in these deformation bands suggest that organic material could also participate in the production of calcite. Microbially mediated precipitation requires organic molecules in the soil solution, which are adsorbed onto the crystal. This adsorption inhibits crystal growth, promoting an acicular morphology [*Verrecchia and Verrecchia*, 1994]. Regardless of the mechanism of calcite precipitation (desiccation or microbially mediated precipitation), the addition of $CaCO_3$ requires preferential fluid flow through deformation bands relative to protolith.

5.3. Oxygen Isotope Enrichment

[43] The stable oxygen isotope ratio ($\delta^{18}O$) of a rock depends mainly on the isotopic composition, salinity, and temperature of the fluids with which the rock interacted during and subsequent to its formation [e.g., *Campbell and Larsen*, 1998]. The stable carbon isotope ratio ($\delta^{13}C$) reflects the source of CO_2 for precipitation or rock formation, such as magmatic fluids, meteoric water, or microbial oxidation of organic matter and methane [*Nelson and Smith*, 1996]. Therefore the stable isotopic signatures of fault zones will be different from protolith if the faults have acted as preferential pathways for water distinct from formation fluids. Sampling and analysis of fault zone wall rock also allows evaluation of whether or not fluids "leaked" from the faults into the surrounding host rock, and if they did leak, how far into the host rock fault-related fluid was transported.

Table 3. Stable Isotope Data and Glass and Smectite Content for Protolith-Deformation Band Sets[a]

Sample Description	$\delta^{18}O$	$\delta^{13}C$	Glass, wt %	Smectite, wt %
Crystallized protolith (bt29)	6.1	−25.9	NA	NA
Footwall boundary (bt116c)	8.9	−25.8	4	0
Deformation band with clay (bt116)	6.7	−25.9	9.6	1.4
Hanging wall boundary (bt116b)	7.1	−25.8	4.7	0
Glassy protolith (bt64)	6.2	−25.7	NA	NA
Footwall boundary (bt8/9a)	11.1	−25.3	70.3	2.9
Deformation band with clay (bt9)	8.5	−25.8	50.5	17.4
Deformation band with clay (bt8)	8.8	−26.0	69.6	7.8
Hanging wall boundary (bt8/9b)	9.3	−26.1	69.3	2.2
Crystallized protolith (bt73)	6.8	−25.8	NA	NA
Footwall boundary (bt74)	7.2	−25.9	3.4	0
Deformation band with carbonate and clay (bt111a)	20.8	−4.9	16	36.5
Hanging wall boundary (bt75)	7.7	−25.8	4	0

[a]NA, not analyzed.

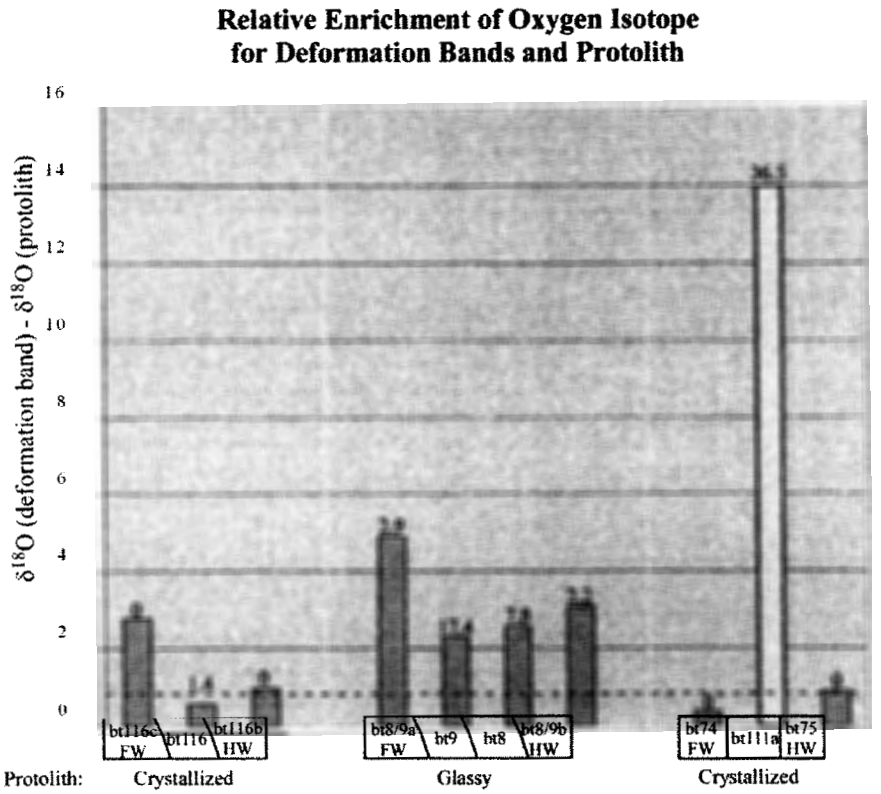

Figure 9. Graph of differences in $\delta^{18}O$ between portions of deformation band fault zones. The $\delta^{18}O$ value for protolith has been subtracted from that of each deformation band analysis such that enrichments are shown as values >0. Schematic representations of fault zone components and approximate fault dips are given below graphed data; FW, footwall; HW, hanging wall. Sample numbers correspond to those given in Table S1. The wt % smectite of each fault zone sample is given above each $\delta^{18}O$ value (vertical bar). Note the lack of a relationship between wt % smectite and $\delta^{18}O$ value. Dashed line represents the limit of precision for determining significant differences between protolith and fault zone $\delta^{18}O$ values. The large difference in $\delta^{18}O$ between deformation band and protolith for sample bt111a results from the presence of calcite in the fault zone. All other samples are dominated by silicates and represent whole rock analysis.

[44] Our data for fault zone material, fault zone boundaries, and protolith indicate a general increase in $\delta^{18}O$ for fault zones with smectite and calcite, especially at the boundaries (Table 3 and Figure 9). These data indicate meteoric fluid-rock interaction within and directly adjacent to deformation bands, which is consistent with low-temperature alteration of the initially high-temperature ignimbrite. However, there is no consistent relationship between wt % smectite and $\delta^{18}O$ value (Figure 9). These data, and the observation that smectite content is higher in fault cores than fault margins, may indicate longer residence times in the cores and higher fluid flux at the fault zone margins where evaporation into high-porosity protolith is more likely to occur. The higher $\delta^{18}O$ values of unaltered fault zone margins (e.g., bt116c; Figure 9) might therefore result from oxygen isotope exchange between the rock and fluids that has not led to chemical diagenesis.

[45] In the calcite-cemented deformation band analyzed, the $\delta^{18}O$ value of 20.8‰ reflects a meteoric fluid source [cf. *Campbell and Larsen*, 1998]. The −9‰ $\delta^{13}C$ value falls within the range of values exhibited by magmatic carbon, which at first consideration suggests that the carbon in this fault is derived from ignimbrite during alteration [cf. *Barnes et al.*, 1978]. However, the amount of magmatic carbon available in rhyolitic ignimbrite like the Bandelier Tuff is very small, and therefore is insufficient for the precipitation of calcite [*Anderson et al.*, 1989; *Blank et al.*, 1993]. Further, this $\delta^{13}C$ value is similar to that reported by *Newman* [1996]. *Newman* [1996] called on local plant roots as the primary source for carbon in the precipitation of calcite in fractures of the Bandelier Tuff; a similar interpretation for calcite in the faults we have studied is consistent with widespread observations of preferential plant root growth in deformation bands [this study; *Lavine et al.*, 2003]. Atmospheric CO_2 input, through dust and rain, may also affect the $\delta^{13}C$ signature within these faults since

they are zones of enhanced fluid flow and translocation [cf. *Ehleringer*, 1988; *Newman*, 1996]. With either of these potential sources of carbon, the stable carbon isotope composition we have measured is consistent with low-temperature, pedogenic precipitation from meteoric fluids.

5.4. Geochemical Differences Between Deformation Bands and Protolith Attributed to Preferential Solute Transport

[46] Trace element concentrations of some deformation bands vary substantially relative to protolith (Table 1). Many of the deformation bands with smectite have higher V, Cr, and/or Cu, concentrations than protolith, which can be attributed to the presence of smectite [*Bhumbla and Keefer*, 1994; *McDonald et al.*, 1996; *Morton et al.*, 2001] and, in one deformation band (bt111b; Table 1), calcite. Higher Ba, As, Th, and U concentrations, found in only a few of these deformation bands (Table 1), can also be linked to calcite and translocated smectite. We infer that the concentrations of these trace elements are higher due to their high affinity for adsorption onto the surfaces of fine-grained smectite and calcite crystals [cf. *Bhumbla and Keefer*, 1994; *McDonald et al.*, 1996]. Dissolution/precipitation processes could facilitate the incorporation of some trace elements into the crystal structures of these diagenetic minerals. Distinct trace element concentrations in deformation bands again support fluid flux, rather than simple fluid retention.

5.5. Implications for Vadose Zone Fluid Flow and Transport in the Bandelier Tuff

[47] Bandelier Tuff units are composed of highly heterogeneous grains and pore spaces. These include macropores (millimeter-scale) in undeformed matrix, micropores (micrometer-scale) in deformation bands in nonwelded units, and fractures (millimeter to centimeter-scale) in welded and crystallized nonwelded units. Fluid flow and transport through these features are of great concern due to the potential for movement of contaminated fluids into the water supply beneath the Pajarito Plateau. This study helps to constrain the role of these structures in vadose zone fluid flow in the Bandelier Tuff.

[48] At most of the locations studied, the Bandelier Tuff has been above the water table since deposition [*Purtymun and Johansen*, 1974]. Although previous workers have suggested that locations in the southern portion of the Pajarito Plateau that are at lower elevations and near canyon bottoms may once have been below the water table [*Purtymun and Johansen*, 1974], the lack of alteration of glass in protolith suggests that the sites we studied in these areas have always been dry. Further, structures in all of the areas studied exhibit similar features, suggesting that fault zone diagenesis occurred under similar conditions. Because of this lack of evidence of saturation, and because reduction of porosity in deformation bands reduces saturated permeability [*Wilson*, 2004], we do not expect these structures to have acted as preferential flow paths below the water table. We therefore infer that preferential alteration and cementation of all fault zones studied record enhanced vadose zone fluid transport through deformation bands.

[49] A remaining question is: what was the direction of preferential fluid flux? *Sigda* [2004] determined the unsaturated hydraulic properties of deformation bands and protolith sand and modeled the impact of the faults on both downward, gravity-driven flow and wicking upward from the water table. The latter is a potentially significant mechanism in thin vadose zones. The shallow water table acts as fluid source; evapotranspiration at the surface provides water demand or tension. The enhanced capillarity of deformation bands (due to small pore size) causes preferential wicking upward of fluid into the fault. This mechanism only occurs in shallow water tables because tension due to surface "demand" decreases with depth; if the water table is deep enough, the process shuts down because the potential difference between the water table and surface is so low. Further, water can be wicked upward through this process only 1–2 m above the water table [*Sigda*, 2004, also personal communication, 2006]. Thus it is not a viable mechanism for fault zone diagenesis on the Pajarito Plateau, where smectite and calcite enrichment of deformation bands is evident near the surface, 152 m from the water table.

[50] Gravity-driven flow through deformation bands is, however, consistent with our data. In arid and semiarid climates, where the residual water content of the protolith is low, gravity-driven vadose zone fluid flow in faulted sand occurs preferentially through deformation bands [*Sigda and Wilson*, 2003]. *Sigda and Wilson* [2003] demonstrate deformation band conductivities that are greater by 2–6 orders of magnitude than those of protolith sand at a range of moisture conditions typical of semiarid and arid vadose zones. This allows 10^2–10^6 times higher moisture transport and solute advection in fault material than parent sands under steady state, one-dimensional, gravity-driven flow. Deformation bands in ignimbrites are zones of reduced grain size resulting in smaller, more regularly shaped pores. Capillary rise is higher in smaller pores; irregularly shaped pores, like those in ignimbrites, make poor capillary tubes [*Birkeland*, 1999]; thus we anticipate that deformation bands in tuffs would, like those in sand, be more conductive in desert vadose zones. We infer that the small grain sizes and large surface area in deformation bands in the Bandelier Tuff facilitated alteration in the presence of water. Downward flow also provides a source for clay and calcite: soil smectite and eolian dust, respectively, both transported by meteoric fluid downward into deformation bands.

[51] Many hydrologic models of fluid flow and solute transport through ignimbrite deposits consider focused flow and transport through fractures in welded units only [e.g., *Winograd*, 1971; *Turin and Rosenberg*, 1996]. Matrix flow is generally assumed to dominate nonwelded units because fractures are sparse, and where present, have been shown through modeling studies to imbibe water through the fracture wall and not allow downward transport of fluids [*Birdsell et al.*, 2005; *Robinson et al.*, 2005]; deformation bands have only recently been documented in these materials [*Wilson et al.*, 2003]. Accordingly, vadose zone fluid flow models predict slow, diffusional flow through nonwelded ignimbrites, and focused, fast fluid flow through fractures in welded ignimbrites [e.g., *Wolfsberg et al.*, 2000]. Data presented here, however, indicate that deformation bands are also zones of focused fluid flow.

[52] Preferential alteration and cementation of deformation bands demonstrates that these structures are preferential

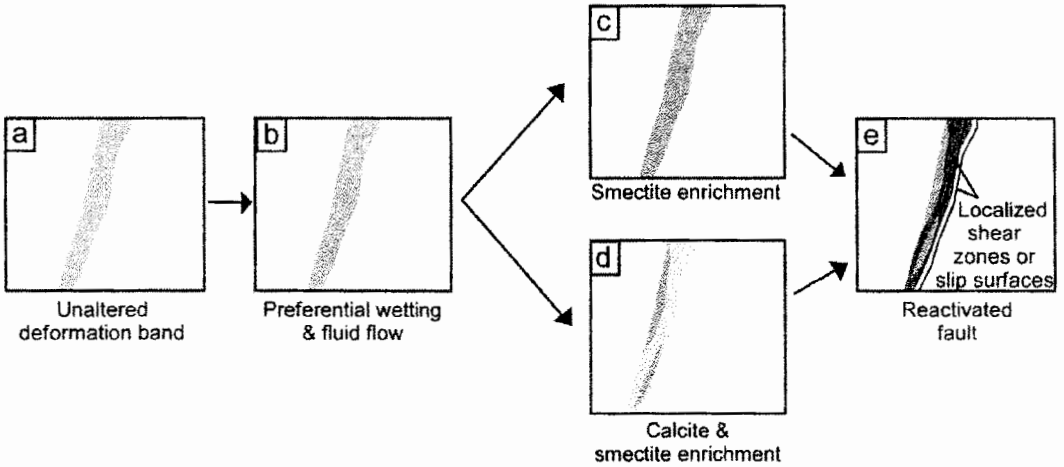

Figure 10. Schematic diagram showing proposed evolution of a deformation band. Unaltered deformation band (Figure 10a) preferentially retains water (Figure 10b) due to pore size reduction in arid vadose zone. Preferential water retention leads to preferential fluid flow during infiltration events. Preferential water retention and fluid flow leads to clay enrichment (Figure 10c) with variable amounts of calcite cementation (Figure 10d). Subsequent reactivation within or along the boundaries of modified deformation bands produces localized shear zones or distinct slip surfaces (Figure 10e). Diagenetic modifications eventually reduce pore size to the extent that they destroy pore connectivity and close the flow pathways. Slip surfaces, roots, and/or desiccation cracks may locally enhance porosity, allowing flow after diagenesis has blocked pathways within deformation bands proper; only slip surfaces are expected to produce continuous flow pathways.

flow pathways. Trace elements such as V, Cr, and Cu may be trapped in the fault zone by fine-grained diagenetic minerals. Other elements may not be trapped, in which case downward transport could occur up to several meters through a deformation band in a nonwelded ignimbrite unit and then through connecting fractures in a welded ignimbrite unit [cf. *Vaniman and Chipera*, 1995], potentially arriving at the regional water table at depth. Vertical communication between deformation bands and fractures requires continuity of a given fault, or connectivity of individual faults in a zone, through successive units of the Bandelier Tuff. This spatial continuity of a fault through variably welded units is observed only locally on the Pajarito Plateau due to the preferential erosion of welded units, which limits exposure. However, a vertically continuous fault cutting variably welded ignimbrite has also been documented at Busted Butte, Nevada [*Wilson et al.*, 2003], suggesting that they are not uncommon. Further, *Riley et al.* [2005] show high densities of faults in nonwelded units adjacent to strands of the Pajarito fault. Faults that traverse multiple mechanical units could be fast paths for fluid flow and mineral/solute transport to far greater depths than previously considered.

5.6. Proposed Model of Structural and Diagenetic Evolution of Deformation Bands in Nonwelded Bandelier Tuff

[53] The results of this work can be expressed in the form of a conceptual model of the structural and diagenetic evolution of deformation band faults on the Pajarito Plateau (Figure 10). In this model, deformation bands begin as zones in which grains, especially thin and weak glass shards, are crushed, and pores collapse by shear-enhanced compaction, grain boundary sliding, and/or shearing (Figures 1b and 10a. Glass shards are preferentially deformed as deformation bands propagate through the weakest portions of the rock. As a result, deformation bands may have slightly more glass and lower quartz, feldspar, tridymite, cristobalite, or trace minerals than protolith. Other than this difference, which is more pronounced in crystallized nonwelded ignimbrite, deformation bands are initially composed of the same material as the protolith, but have lower porosity, smaller grains, and smaller pore sizes [*Wilson et al.*, 2003]. In dry vadose zones, these petrophysical properties cause similar faults in sand to be zones of preferential water retention (Figure 10b) [*Stephens*, 1996; *Sigda et al.*, 1999; *Sigda and Wilson*, 2003]. This preferential water retention leads to enhanced alteration of unstable and grain-size-reduced feldspar, mafic lithic clasts, and volcanic glass [cf. *Starkey and Blackmon*, 1979; cf. *Hay and Guldman*, 1987; cf. *Lander and Hay*, 1993], forming smectite (Figures 3 and 10c). Preferential water retention in faulted nonwelded ignimbrites also leads to enhanced fluid flow during infiltration events, allowing downward colloidal transport of soil-derived smectite and Ca-rich eolian dust from the surface [cf. *Wan and Wilson*, 1994; *Eberly et al.*, 1996]. In situ alteration is facilitated by the heightened reactivity of grain-size-reduced ignimbrite, and allows for extensive accumulation of smectite within deformation bands (Figures 3, 10b, and 10c). Preferentially wet zones in arid environments are also observed to be zones of preferential root growth. In our conceptual model, fluid retention, plant roots, and smectite within a deformation band lead to precipitation of calcite by

microbial or episodic desiccation activity (Figures 3 and 10d) [cf. *Boquet et al.*, 1973; *Verrecchia and Verrecchia*, 1994; *Newman et al.*, 1997].

[54] Continued alteration of, and precipitation within, deformation bands will further reduce pore size, eventually closing pore throats [cf. *Mok et al.*, 2002], at which point the diagenetically modified deformation band will become a barrier to vadose zone fluid flow (Figures 10c and 10d). Further structural modification of the deformation band, such as opening of large desiccation cracks in smectite, may again lead to localized pathways for fluids (Figure 10e). Reactivation of a deformation band can follow the development of a weak, clay-rich fault core and/or relatively rigid calcite layers that may fracture and accommodate greater slip. Therefore the presence of smectite or calcite in these faults can create complex fault zone architectures, both in terms of fault zone structural elements and permeability. In a larger tectonic context, as these faults are progressively buried with time and/or the rock is saturated, desiccation cracks close. Fault zone smectite and calcite reduce saturated fluid flow and localize deformation, effectively halting further development of deformation bands. Vadose zone alteration therefore is one way to produce a clay-rich fault core at early stages in a fault's history, resulting in fault zone weakening and localization of deformation.

6. Conclusions

[55] Deformation bands in both glassy and crystallized nonwelded units of the Bandelier Tuff are zones of preferential smectite enrichment and calcite cementation. Preferential vadose zone fluid flow through these bands of pore and grain size reduction is recorded by these diagenetic phases, by microstructures, and by differences in chemistry between deformation bands and protolith.

[56] Smectite enrichment in deformation bands is the result of a combination of in situ alteration of unstable volcanic glass, alkali feldspar, and mafic minerals in the presence of water and colloidal transport (translocation) of soil-derived smectite from the surface. Alteration is facilitated by the heightened reactivity of grain-size-reduced ignimbrite. These combined processes require both greater fluid retention and preferential flow through deformation bands relative to adjacent, smectite-poor protolith.

[57] Calcite cement in deformation bands consists of rod-shaped microcrystallites that form by microbially mediated precipitation and physicochemical processes associated with repeated desiccation of clay. Preferential root growth through faults and calcite micromorphology consistent with biologic activity collectively suggest that water is preferentially retained in these structures. The observed increase in calcite in these deformation bands relative to protolith via pedogenic dissolution/precipitation-mediated transport of Ca-rich eolian dust also requires enhanced fluid flow.

[58] The elemental geochemistry of deformation bands changes with alteration and cementation. V, Cr, and Cu are most consistently found in higher amounts in altered and cemented deformation bands relative to protolith. Major oxide contents also vary; Fe_2O_3 and MgO, for example, are typically higher in deformation bands containing smectite and CaO is higher in deformation bands with calcite; SiO_2, Na_2O, and K_2O are consistently lower in faults with >10 wt % smectite. Changes in the amounts of these constituents with diagenesis record higher fluid flux in deformation bands relative to protolith.

[59] Across the Pajarito Plateau, small-displacement faults may number in the thousands over a km^2 area [*Carter and Winter*, 1995]. Although the nature of the faults that *Carter and Winter* [1995] studied has not been determined, many occur in nonwelded ignimbrite, and therefore may be deformation bands rather than fractures. Adjacent to the main strands of the Pajarito fault system, these deformation bands can occur in densities of more than 6 in a 10 m transect [*Riley et al.*, 2005]. Given the evidence of the effect of deformation bands on vadose zone fluid flow and transport, we suggest that where they are sufficiently continuous and densely spaced, these recently documented structures may be significant vadose zone pathways for recharge and contaminant transport.

[60] **Acknowledgments.** This research has been funded by a grant through the Institute of Geophysics and Planetary Physics (IGPP) at Los Alamos National Laboratory. Additional funding was provided by the Wyoming Geological Association (J. David Love Field Scholarship) and the New Mexico Geological Society (Grant-in-Aid). Thanks to Nelia Dunbar and Lynn Heizler for assistance on the electron microprobe, Steve Chipera for XRD analyses, Andrew Campbell for stable isotope analyses, Chris McKee for XRF analyses, Randy Korotev for INA analyses, and members of the Faults and Fluids group at New Mexico Tech for useful discussions. We also thank Jim Evans, John C. Mutter, and an anonymous reviewer for their useful reviews, which we agree improved the paper significantly.

References

Aldrich, M. (1986), Tectonics of the Jemez Lineament in the Jemez Mountains and Rio Grande Rift, *J. Geophys. Res.*, *91*(B2), 1753–1762.

Anderson, A. T., S. Newman, S. Williams, T. Druitt, C. Skirius, and E. Stolper (1989), H_2O, CO_2, Cl and gas in the Plinian and ash-flow Bishop rhyolite, *Geology*, *17*, 221–225.

Antonellini, M., and A. Aydin (1994), Effect of faulting on fluid flow in porous sandstones: Petrophysical properties, *AAPG Bull.*, *78*, 355–377.

Aronson, E. C. (1999), Modeling investigations on gas permeameters: Spatial weighting functions and layered systems, M. S. thesis, 91 pp., N. M. Inst. of Min. and Technol., Socorro.

Aydin, A., and A. Johnson (1978), Development of faults as zones of deformation bands and as slip surfaces in sandstones, *Pure Appl. Geophys.*, *116*, 931–942.

Barnes, I., J. R. O'Neil, and J. J. Trescases (1978), Present day serpentinization in New Caledoniia, Oman, and Yugoslavia, *Geochim. Cosmochim. Acta*, *42*, 144–145.

Birdsell, K. H., B. D. Newman, D. E. Broxton, and B. A. Robinson (2005), Conceptual models of vadose zone flow and transport beneath the Pajarito Plateau, Los Alamos, New Mexico, *Vadose Zone J.*, *4*, 620–636.

Bhumbla, D. K., and R. F. Keefer (1994), Arsenic mobilization and bioavailability in soils, in *Arsenic in the Environment, Part I: Cycling and Characterization*, edited by J. O. Nrlagu, pp. 51–82, John Wiley, Hoboken, N. J.

Birkeland, P. W. (1999), *Soils and Geomorphology*, 3rd ed., 430 pp., Oxford Univ. Press, New York.

Blank, J. G., E. M. Stolper, and M. R. Carroll (1993), Solubilities of carbon dioxide and water in rhyolitic melt at 850°C and 750 bars, *Earth Planet. Sci. Lett.*, *119*, 27–36.

Boquet, E., A. Boronat, and A. Ramos-Cormenzana (1973), Production of calcite (calcium carbonate) crystals by soil bacteria is a general phenomenon, *Nature*, *246*, 527–529.

Broxton, D., G. Heiken, S. J. Chipera, and F. M. Byers (1995), Stratigraphy, petrography, and mineralogy of Bandelier Tuff and Cerro Toledo deposits, in *Earth Science Investigations for Environmental Restoration—Los Alamos National Laboratory Technical Area 21*, edited by D. E. Broxton and P. G. Eller, *Los Alamos Natl. Lab. Rep., LA-12934-MS*, 33–64.

Caine, J. S., J. P. Evans, and C. B. Forster (1996), Fault zone architecture and permeability structure, *Geology*, *24*, 1025–1028.

Campbell, A. R., and P. Larsen (1998), Introduction to stable isotope applications in hydrothermal systems, in *Techniques in Hydrothermal Ore Deposit Geology, Rev. Econ. Geol.*, vol. 10, edited by J. Richardson and P. Larsen, pp. 173–193, Soc. of Econ. Geol., Tulsa, Okla.

Carter, K. E., and J. N. Gardner (1995), Quaternary fault kinematics in the northwestern Española Basin, Rio Grande Rift, New Mexico, in *Geology of the Santa Fe Region, Field Conf. Guideb. N. M. Geol. Soc., 46th*, 97–102.

Carter, K. E., and C. L. Winter (1995), Fractal nature and scaling of normal faults in the Espanola Basin, Rio Grande Rift, New Mexico: Implications for fault growth and brittle strain, *J. Struct. Geol., 17*(6), 863–873.

Cashman, S., and K. Cashman (2000), Cataclasis and deformation-band formation in unconsolidated marine terrace sand, Humboldt County, California, *Geology, 28*, 111–114.

Chipera, S. J., and D. L. Bish (2002), FULLPAT: A full-pattern quantitative analysis program for X-ray powder diffraction using measured and calculated patterns, *J. Appl. Crystallogr., 35*, 744–749.

Chipera, S. J., G. D. Guthrie Jr., and D. L. Bish (1993), Preparation and purification of mineral dusts, in *Health Effects of Mineral Dusts, Rev. Mineral.*, vol. 28, edited by G. D. Guthrie Jr. and B. T. Mossman, pp. 235–249, Mineral. Soc. of Am., Washington, D. C.

Davenport, D. W., B. P. Wilcox, and B. L. Allen (1995), Micromorphology of pedogenically derived fracture fills in Bandelier Tuff, New Mexico, *Soil Sci. Soc. Am. J., 59*, 1672–1683.

Dinwiddie, C. L., R. W. Fedors, D. A. Ferrill, and K. Keighley-Bradbury (2002), Matrix permeabilities of faulted nonwelded tuffs, *Geol. Soc. Am. Abstr. Programs, 34*(6), 309.

Dunn, D. E., L. J. Lafountain, and R. E. Jackson (1973), Porosity dependence and mechanism of brittle faulting in sandstone, *J. Geophys. Res., 78*, 2303–2317.

Eberly, P., L. D. McFadden, and P. M. Watt (1996), Eolian dust as a factor in soil development on the Pajarito Plateau, Los Alamos area, northern New Mexico, in *The Jemez Mountains Region*, edited by F. Goff et al., *Field Conf. Guideb. N. M. Geol. Soc., 47th*, 383–389.

Ehleringer, J. R. (1988), Carbon isotope ratios and physiological processes in aridland plants, in *Applications of Stable Isotope Ratios to Ecological Research, Ecol. Ser. Monogr.*, vol. 62, edited by P. W. Rundel, J. R. Ehleringer, and K. A. Nagy, pp. 41–54, Springer, New York.

Evans, J. P., and K. K. Bradbury (2004), Faulting and fracturing of nonwelded Bandelier Tuff, eastern California: Deformation mechanisms in very porous materials in the vadose zone, *Vadose Zone J., 3*, 602–623.

Evans, J. P., and F. M. Chester (1995), Fluid-rock interaction in faults of the San Andreas system: Inferences from San Gabriel fault rock geochemistry and microstructures, *J. Geophys. Res., 100*, 13,007–13,020.

Freundt, A., C. J. N. Wilson, and S. N. Carey (2000), Ignimbrites and block-and-ash flow deposits, in *Encyclopedia of Volcanoes*, pp. 581–599, Elsevier, New York.

Gardner, J. N., and L. House (1987), Seismic hazards investigations at Los Alamos National Laboratory, 1984–1985, *Los Alamos Natl. Lab. Rep., LA-11072-MS*, 76 pp.

Gile, L. H., J. W. Hawley, and R. Grossman (1981), *Soils and Geomorphology in the Basin and Range Area of Southern New Mexico, Guidebook to the Desert Project, Mem. N. M. Bur. Mines Miner. Resour., 39*, 222 pp.

Gile, L. H., J. W. Hawley, R. Grossman, H. C. Monger, C. E. Montoya, and G. H. Mack (1995), Supplement to the Desert Project Guidebook, with emphasis on soil micromorphology, *N. M. Bur. Mines Miner. Resour. Bull., 142*, 96 pp.

Grant, J. A. (1986), The isocon diagram—A simple solution to Gresens' equation for metasomatic alteration, *Econ. Geol., 81*, 1976–1982.

Gresens, R. L. (1967), Composition-volume relationships of metasomatism, *Chem. Geol., 2*, 47–65.

Hallet, R. B., and P. R. Kyle (1993), XRF and INAA Determinations of major and trace elements in Geological Survey of Japan igneous and sedimentary rock standards, *Geostand. Newsl., 17*, 127–134.

Hay, R. L., and S. G. Guldman (1987), Diagenetic alteration of silicic ash in Searles Lake, CA, *Clays Clay Miner., 35*(6), 449–457.

Heiken, G., F. Goff, J. Gardner, W. Baldridge, J. Hulen, D. Nielson, and D. Vaniman (1990), The Valles/Toledo Caldera Complex, Jemez Volcanic Field, New Mexico, *Annu. Rev. Earth Planet. Sci., 18*, 27–53.

Izett, G. A., and J. D. Obradovich (1994), $^{40}Ar/^{39}Ar$ age constraints on the Jaramillo normal subchron and the Matuyama-Bruhnes geomagnetic boundary, *J. Geophys. Res., 99*, 2925–2934.

Knipe, R. J. (1993), The influence of fault zone processes and diagenesis on fluid flow, in *Diagenesis and Basin Development*, edited by A. D. Horbury and A. G. Robinson, *AAPG Stud. Geol., 36*, 135–148.

Korotev, R. L. (1991), Geochemical stratigraphy of two regolith cores from the central highlands of the Moon, *Proc. Lunar Planet. Sci., 21*, 229–289.

Lander, R. H., and R. L. Hay (1993), Hydrogeologic control on zeolitic diagenesis of the White River sequence, *Geol. Soc. Am. Bull., 105*, 361–376.

Lavine, A., C. J. Lewis, D. K. Katcher, J. N. Gardner, and J. E. Wilson (2003), Geology of the north-central to northeastern portion of Los Alamos National Laboratory, New Mexico, *Los Alamos Natl. Lab. Rep., LA-14043-MS*, 44 pp.

Lewis, C. J., A. Lavine, S. L. Reneau, J. N. Gardner, R. Channell, and C. W. Criswell (2002), Geology of the western part of Los Alamos National Laboratory (TA-3 to TA-16), Rio Grande Rift, New Mexico, *Los Alamos Natl. Lab. Rep., LA-13960-MS*, 97 pp.

McCrea, J. M. (1950), The isotopic chemistry of carbonates and a paleotemperature scale, *J. Chem. Phys., 18*, 849–857.

McDonald, E. V., P. A. Longmire, P. M. Watt, R. T. Ryti, and S. L. Reneau (1996), Natural and major trace element background geochemistry of selected soil profiles, Los Alamos, New Mexico, in *The Jemez Mountains Region*, edited by F. Goff et al., *Field Conf. Guideb. N. M. Geol. Soc., 47th*, 375–382.

Mok, U., Y. Bernabé, and B. Evans (2002), Permeability, porosity and pore geometry of chemically altered porous silica glass, *J. Geophys. Res., 107*(B1), 2015, doi:10.1029/2001JB000247.

Monger, H. C., and H. P. Adams (1996), Micromorphology of calcite-silica deposits, Yucca Mountain, Nevada, *Soil Sci. Soc. Am. J., 60*(2), 519–530.

Morton, J. D., J. D. Semrau, and K. F. Hayes (2001), An X-ray absorption spectroscopy study of the structure and reversibility of copper absorbed to montmorillonite clay, *Geochem. Cosmochem. Acta, 65*, 2709–2722.

Mozley, P. S., and L. B. Goodwin (1995), Patterns of cementation along a Cenozoic normal fault: A record of paleoflow orientations, *Geology, 23*, 539–542.

Nakamura, N. (1974), Determination of REE, Ba, Fe, Mg, Na, and K in carbonaceous and ordinary chondrites, *Geochim. Cosmochim. Acta, 38*, 757–775.

Nelson, C. S., and A. H. Smith (1996), Stable oxygen and carbon isotope compositional fields for skeletal and diagenetic components in New Zealand Cenozoic nontropical carbonate sediments and limestones: A synthesis and review, *N. Z. J. Geol. Geophys., 39*, 93–107.

Newman, B. D. (1996), Geochemical investigations of calcite fracture fills and mesa-top water dynamics on the Pajarito Plateau, New Mexico, Ph.D. thesis, 254 pp., N. M. Inst. of Min. and Technol., Socorro.

Newman, B. D., A. R. Campbell, D. I. Norman, and D. B. Ringelberg (1997), A model for microbially induced precipitation of vadose-zone calcites in fractures at Los Alamos, New Mexico, USA, *Geochim. Cosmochim. Acta, 61*, 1783–1792.

Purtymun, W. (1995), Geologic and hydrologic records of observation wells, test holes, test wells, supply wells, springs, and surface water stations in the Los Alamos area, *Los Alamos Natl. Lab. Rep., LA-12883-MS*, 339 pp.

Purtymun, W. D., and S. Johansen (1974), General geohydrology of the Pajarito Plateau, in *Ghost Ranch, Field Conf. Guideb. N. M. Geol. Soc., 25th*, 347–349.

Quade, J., and T. E. Cerling (1990), Stable isotopic evidence for a pedogenic origin of carbonates in trench 14 near Yucca Mountain, Nevada, *Science, 250*, 1549–1552.

Rawling, G., L. B. Goodwin, and J. Wilson (2001), Internal architecture, permeability structure, and hydrologic significance of contrasting fault zone types, *Geology, 29*, 43–46.

Riley, P., L. B. Goodwin, and C. J. Lewis (2005), Spatial distribution of deformation bands in the Pajarito fault zone, New Mexico: Implications for vadose zone fluid flow, *Geol. Soc. Am. Abstr. Programs, 37*, 374.

Robinson, B. A., S. G. McLin, and H. S. Viswanathan (2005), Hydrologic behavior of unsaturated, fractured tuff: Interpretation and modeling of a wellbore injection test, *Vadose Zone J., 4*, 694–707.

Sigda, J. M. (2004), Preferential flow and transport through deformation band faults in the semi-arid vadose zone of the Rio Grande Rift, New Mexico, USA, Ph.D. thesis, 300 pp., N. M. Inst. of Min. and Technol., Socorro.

Sigda, J. M., and J. L. Wilson (2003), Are faults preferential flow paths through semiarid and arid vadose zones?, *Water Resour. Res., 39*(8), 1225, doi:10.1029/2002WR001406.

Sigda, J. M., L. B. Goodwin, P. S. Mozley, and J. L. Wilson (1999), Permeability alteration in small-displacement faults in poorly consolidated sediments: Rio Grande Rift, central New Mexico, in *Faults and Subsurface Fluid Flow in the Shallow Crust, Geophys. Monogr. Ser.*, vol. 113, edited by W. C. Haneberg et al., pp. 51–68, AGU, Washington, D. C.

Smith, R. L., and R. A. Bailey (1966), The Bandelier Tuff—A study of ash-flow eruption cycles from zoned magma chambers, *Bull. Volcanol., 29*, 83–104.

Sommer, M. A. (1977), Volatiles H_2O, CO_2, and CO in silicate melt inclusions in quartz phenocrysts from the rhyolitic Bandelier air-fall and ash-flow tuff, New Mexico, *J. Geol., 85*(4), 423–432.

Starkey, H. C., and P. D. Blackmon (1979), Clay mineralogy of Pleistocene Lake Tecopa, Inyo County, California, *U.S. Geol. Surv. Prof. Pap., 1061*, 34 pp.

Stephens, D. B. (1996), *Vadose Zone Hydrology*, 347 pp., Lewis Publ., Boca Raton, Fla.

Stimac, J., D. Hickmott, R. Abell, A. C. L. Larocque, D. Broxton, J. Gardner, S. Chipera, J. Wolff, and E. Gauerke (1996), Redistribution of Pb and other volatile trace metals during eruption, devitrification, and vapor-phase crystallization of the Bandelier Tuff, New Mexico, *J. Volcanol. Geothermal Res.*, *73*, 245–266.

Stimac, J. A., D. E. Broxton, E. C. Kluk, S. J. Chipera, and J. R. Budahn (2002), Stratigraphy of the tuffs from borehole 49-2-700-1 at Technical Area 49, Los Alamos National Laboratory, New Mexico, *Los Alamos Natl. Lab. Rep.*, *LA-13969*, 14 pp.

Tidwell, V. C., and J. L. Wilson (2000), Heterogeneity, permeability patterns, and permeability upscaling: Physical characterization of a block of Massillon sandstone exhibiting nested scales of heterogeneity, *SPE Res. Eval. Eng.*, *3*(4), 283–291.

Tobin, H., P. Vannucchi, and M. Meschede (2001), Structure, inferred mechanical properties, and implications for fluid transport in the decollement zone, Costa Rica convergent margin, *Geology*, *29*, 907–910.

Turin, H. J., and N. D. Rosenberg (1996), A conceptual model for flow in the vadose zone beneath the finger mesas of the Pajarito Plateau, in *The Jemez Mountains Region*, edited by F. Goff et al., *Field Conf. Guideb. N. M. Geol. Soc.*, *47th*, 74–76.

Vaniman, D. T., and S. J. Chipera (1995), Mesa-penetrating fractures, fracture mineralogy, and projected fault traces at Pajarito Mesa, in *Geological Site Characterization for the Proposed Mixed Waste Disposal Facility, Los Alamos National Laboratory*, edited by S. L. Reneau and R. Raymond Jr., *Los Alamos Natl. Lab. Rep.*, *LA-13089-MS*.

Vaniman, D. T., S. J. Chipera, D. L. Bish, M. C. Duff, and D. B. Hunter (2002), Crystal chemistry of clay-Mn oxide associations in soils, fractures, and matrix of the Bandelier Tuff, Pajarito Mesa, New Mexico, *Geochim. Cosmochim. Acta*, *66*, 1349–1374.

Verrecchia, E. P., and K. E. Verrecchia (1994), Needle-fiber calcite: A critical review and a proposed classification, *J. Sediment. Res., Sect. A*, *64*(3), 650–664.

Wallace, P. J., A. T. Anderson Jr., and A. M. Davis (1999), Gradients in H_2O, CO_2, and exsolved gas in a large-volume silicic magma system: Interpreting the record preserved in melt inclusions from the Bishop Tuff, *J. Geophys. Res.*, *104*, 20,097–20,122.

Wan, J., and J. L. Wilson (1994), Colloid transport in unsaturated porous media, *Water Resour. Res.*, *30*(4), 857–864.

Wilson, J. E. (2004), Characteristics of faults in nonwelded ignimbrites from the Pajarito Plateau and implications for fluid flow, Ph.D. thesis, 194 pp., N. M. Inst. of Min. and Technol., Socorro.

Wilson, J. E., L. B. Goodwin, and C. J. Lewis (2003), Deformation bands in nonwelded ignimbrites: Petrophysical controls on fault-zone deformation and evidence of preferential fluid flow, *Geology*, *31*, 837–840.

Winograd, I. J. (1971), Hydrogeology of ash flow tuff: A preliminary statement, *Water Resour. Res.*, *7*(4), 994–1006.

Wohletz, K. (1996), Fracture characterization of the Bandelier Tuff in OU-1098 (TA-2 and TA-41), *Los Alamos National Laboratory Report* LA-13194–MS, 19 pp.

Wolfsberg, A., K. Campbell, and Fabryka-Martin (2000), Use of chlorine-36 to evaluate fracture flow and transport models at Yucca Mountain, Nevada, in *Dynamics of Fluids in Fractured Rock*, *Geophys. Monogr. Ser.*, vol. 122, edited by B. Faybishenko et al., pp. 346–362, AGU, Washington, D. C.

L. B. Goodwin, Department of Geology and Geophysics, University of Wisconsin–Madison, Madison, WI 53711, USA.

C. Lewis, Los Alamos National Laboratory, EES-9, Los Alamos, NM 87545, USA.

J. E. Wilson, Department of Geological Sciences, University of Texas at Austin, Austin, TX 78712, USA. (thejenwilson@hotmail.com)